Title
Synthetic Evaluation of Infrasonic Multipole Waveform Inversion

Journal
Journal of Geophysical Research: Solid Earth, 127(1)

ISSN
2169-9313

Authors
Iezzi, Alexandra M
Matoza, Robin S
Fee, David
et al.

Publication Date
2022

DOI
10.1029/2021jb023223

JGR Solid Earth

RESEARCH ARTICLE
10.1029/2021JB023223

Synthetic Evaluation of Infrasonic Multipole Waveform Inversion

Alexandra M. Iezzi[1], Robin S. Matoza[1], David Fee[2], Keehoon Kim[3], and Arthur D. Jolly[4]

[1]Department of Earth Science and Earth Research Institute, University of California, Santa Barbara, CA, USA, [2]Alaska Volcano Observatory and Wilson Alaska Technical Center, Geophysical Institute, University of Alaska Fairbanks, Fairbanks, AK, USA, [3]Lawrence Livermore National Laboratory, Livermore, CA, USA, [4]U.S. Geological Survey, Hawaiian Volcano Observatory, Hilo, HI, USA

Key Points:

- We investigate the ability to resolve multipole acoustic sources using infrasound waveform inversion methods for a variety of scenarios
- A monopole inversion yields results that may be sufficient for practical purposes, even for multipole sources with a small dipole component
- Synthetic inversion studies can increase understanding of the limitations of multipole infrasound inversions based on deployment scenarios

Correspondence to:

A. M. Iezzi,
amiezzi@ucsb.edu

Citation:

Iezzi, A. M., Matoza, R. S., Fee, D., Kim, K., & Jolly, A. D. (2022). Synthetic evaluation of infrasonic multipole waveform inversion. *Journal of Geophysical Research: Solid Earth*, *127*, e2021JB023223. https://doi.org/10.1029/2021JB023223

Received 10 SEP 2021
Accepted 23 DEC 2021

Abstract

Acoustic source inversions estimate the mass flow rate of volcanic explosions or yield of chemical explosions and provide insight into potential source directionality. However, the limitations of applying these methods to complex sources and their ability to resolve a stable solution have not been investigated in detail. We perform synthetic infrasound waveform inversions that use 3-D Green's functions for a variety of idealized and realistic deployment scenarios using both a flat plane and Yasur volcano, Vanuatu as examples. We investigate the ability of various scenarios to retrieve the input source functions and relative amplitudes for monopole and multipole (monopole and dipole) inversions. Infrasound waveform inversions appear to be a robust method to quantify mass flow rates from simple sources (monopole) using deployments of infrasound sensors placed around a source, but care should be taken when analyzing and interpreting results from more complex acoustic sources (multipole) that have significant directional components. In the examples we consider the solution is stable for monopole inversions with a signal-to-noise ratio greater than five and the dipole component is small. For most scenarios investigated, the vertical dipole component of the multipole explosion source is poorly constrained and can impact the ability to recover the other source term components. Because multipole inversions are ill-posed for many deployments, a low residual does not necessarily mean the proper source vector has been recovered. Synthetic studies can help investigate the limitations and place bounds on information that may be missing using monopole and multipole inversions for potentially directional sources.

Plain Language Summary

Explosions such as those from volcanoes create low-frequency sound below the threshold of human hearing (infrasound) that can be recorded at a variety of distances. Infrasound can be used to calculate the amount of material being ejected from a volcano and if the sound waves are preferentially emitted in a certain direction. However, this directionality can be difficult to determine because infrasound sensors are often placed on the ground surface, which makes determining the vertical directionality of an explosion source difficult. We use numerical model examples of infrasound deployments around a volcanic source and vary parameters including the station locations, noise level, strength of directionality, and impact of wind to investigate the ability to recover the input source parameters. We find that assuming an infrasound source radiates equally in all directions is good enough even for directional sources if the directional component is small and the signal is five times higher in amplitude than the noise. However, caution should be used for sources that are directional for many infrasound sensor deployments.

1. Introduction

Accurate quantification of explosion parameters including those from volcanoes and anthropogenic sources is vital for volcanic hazard monitoring and global security. An increasingly popular method to estimate the size or yield of explosion signals is using measurements of infrasound, or low frequency sound waves (below 20 Hz). Infrasound can be used to detect, locate, characterize, and quantify acoustic sources at a variety of distances (De Angelis et al., 2019; Fee & Matoza, 2013; Matoza et al., 2019) and unlike other remote sensing techniques, it is largely unaffected by cloud cover. Infrasound recordings of explosion signals can also be combined with multi-disciplinary observations such as seismic data in order to better understand shallow to subaerial explosion sources (e.g., Blom et al., 2020; Iezzi et al., 2020).

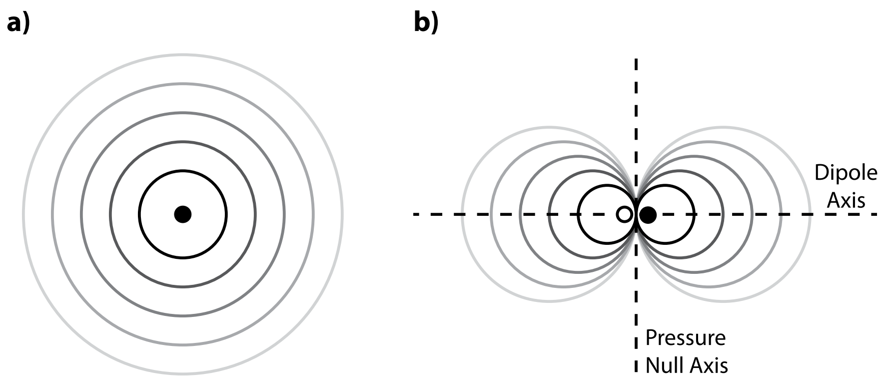

Figure 1. Acoustic radiation pattern resulting from a (a) monopole and (b) dipole source. Positive and negative monopole sources are represented by black and white circles, respectively, and the pressure field emitted is represented by contours with decreasing amplitude from dark to light. Figure reproduced from Iezzi et al. (2019) with permission.

1.1. Acoustic Directionality

In linear acoustic theory, if the source region is compact (i.e., small compared to the acoustic wavelength of interest), the source can be represented as the sum of equivalent point sources (Kim et al., 2012; Lighthill, 1952; Matoza et al., 2013; Pierce, 1989), where the multipole source mechanism is a combination of pressure fluctuations resulting from monopole, dipole, and higher order acoustic sources (Lighthill, 1952). The most simple source (monopole) represents the net change of mass flow rate in a compact source region, generating sound that radiates equally in all directions (Figure 1a). The dipole source is equivalent to force or momentum changes within the fluid (here the air) with no net introduction of fluid and can be represented by two closely spaced (with respect to the acoustic wavelength) monopoles that are out of phase by 180° (Figure 1b) (Pierce, 1989). An acoustic dipole results in directivity of the acoustic radiation pattern, where the maximum pressure change exists along the dipole axis and there is zero pressure change orthogonal to the dipole axis (Lighthill, 1952). Furthermore, dipole sources can be combined to form higher order source terms including lateral and longitudinal quadrupoles.

While many anthropogenic and volcanic explosions appear to be well-characterized by a simple volumetric source, more complex sources including buried chemical explosions (e.g., Blom et al., 2020; Kim et al., 2020), complex volcanic explosions (e.g., Iezzi et al., 2019; Johnson et al., 2008; Jolly et al., 2017), or mass movements (e.g., Johnson et al., 2021) may require a directional source component. Unfortunately, most infrasound sensors are placed on Earth's surface, thus the full acoustic radiation pattern in field studies is not adequately sampled (e.g., Matoza et al., 2013). While this may be sufficient for monopole sources where radiation is isotropic, it is not satisfactory for directional sources with unknown radiation patterns. One key outcome from Matoza et al. (2013) is that typical volcano acoustic data of vertically directional sources better represent a point measurement of acoustic intensity at a particular angle due to this limited sampling, rather than a measure of acoustic power which requires an integration across all angles. Thus, source size estimates such as mass flow rate of a volcanic eruption or yield of an anthropogenic explosion may not be correctly recovered due to inadequate sampling of the potentially directional radiation pattern. Kim et al. (2012) showed that horizontal infrasound directivity at Tungurahua volcano, Ecuador was in good agreement with the opening direction of the vent and Jolly et al. (2016) connected infrasound directivity with video observations from bubble burst eruptions in the crater lake of White Island, New Zealand. Additionally, recent studies by Jolly et al. (2017) and Iezzi et al. (2019) have shown that acoustic directionality from volcanic eruptions are consistent with ballistic directionality at Yasur volcano, Vanuatu (Fitzgerald et al., 2020), which may equate to increased hazard in some azimuths around the volcano.

To increase vertical sensor coverage surrounding an acoustic source, recent studies have explored the potential of placing infrasound sensors on tethered aerostats (e.g., Iezzi et al., 2019; Jolly et al., 2017; Krishnamoorthy et al., 2018, 2019), solar balloons (e.g., Bowman & Lees, 2015; Lamb et al., 2018), or leveraging nearby topography (e.g., McKee et al., 2017; Rowell et al., 2014). However, this is not feasible for most deployments nor generally practical for hazard assessment purposes. Because of this, there is a need to quantify the information that might be missing using sensors placed on the ground surface in order to accurately characterize explosion signals, offering practical implications for improved hazard monitoring.

1.2. Influence of Topography

For a simple point source within a uniform medium, theoretical prediction based on geometrical spreading indicates that the signal amplitude decreases as the inverse of the distance from the source (1/*r*). However, many studies in the past decade have established that strong departures from this theoretical decay model are often observed (e.g., Johnson, 2019), especially in environments such as volcanoes where topography is complex (e.g., Lacanna & Ripepe, 2013) and winds can be strong (e.g., Johnson et al., 2012). Furthermore, the recorded infrasound waveform can be influenced by near-source topography including the crater rim (Kim & Lees, 2011; Matoza et al., 2009) which should be accounted for prior to making interpretations about the source mechanism. A standard method for constraining the effects of topography on acoustic propagation is to use the Finite-Difference Time-Domain (FDTD) numerical modeling method (e.g., de Groot-Hedlin, 2016; Kim & Lees, 2011, 2014; Lacanna & Ripepe, 2013, 2020; Matoza et al., 2009; Petersson & Sjögreen, 2018), which has been tailored to both personal computers and high performance machines. Other methods that have been used to model the impact of topography at local distances include a thin screen approximation (amplitude information only, Ishii et al., 2020; Maher et al., 2021), simple Quasi-1D method (Watson et al., 2019), and more computationally intensive spectral element methods (e.g., Brissaud et al., 2017; Martire et al., 2021).

Neglecting the effect of topography on recorded infrasound data can lead to inaccurate interpretations of the explosion source, especially for volcanoes where topography is pronounced. Kim et al. (2015) found that not accounting for topography for source inversions can lead to underestimation of the total volume flow rate solution by a factor of 2 for explosions at Sakurajima volcano, Japan. Additionally, it has been found that accounting for topography using 3-D Green's functions can improve source localization techniques, including the Time-Reversal Mirror (Kim & Lees, 2014) and Reverse Time Migration (Fee et al., 2021) algorithms.

1.3. Infrasound Waveform Inversion Studies

Infrasound waveform inversion methods are being developed to investigate the source mechanisms of volcanic and anthropogenic explosions. Many infrasound waveform inversion studies focus on an inversion using only a monopole source and have been used to provide an accurate measure of volume and mass flow rates for volcanic explosions (e.g., Fee et al., 2017; Johnson et al., 2008; Johnson & Miller, 2014; Kim et al., 2015) which are invaluable parameters for volcano monitoring and ash transport models, as well as yield for anthropogenic explosions (e.g., Kim et al., 2018; Kim & Rodgers, 2016). These studies have obtained excellent waveform fits, with residuals of ~0.05, although higher order source terms, such as the dipole, may be present even for simple volcanic and anthropogenic explosions. With increased network coverage, some studies have further attempted to constrain the potential directional radiation pattern of the acoustic source by performing multipole inversions for volcanic explosions (De Angelis et al., 2016; Diaz-Moreno et al., 2019; Iezzi et al., 2019; Johnson et al., 2008; Kim et al., 2012), which may be linked to preferentially directed hazards such as ballistics (Jolly et al., 2017).

Early infrasound source inversion studies assumed simple 1-D Green's functions for acoustic propagation in a half space (e.g., De Angelis et al., 2016; Johnson et al., 2008; Johnson & Miller, 2014; Kim et al., 2012). However, multipole inversions that do not account for the effects of topography may yield an "induced" or "effective" dipole solution (Kim et al., 2012), which is different than the standard acoustic dipole source (i.e., two closely spaced monopole sources that are out of phase). A well-known example from hydroacoustics and marine geophysics of an effective or induced dipole is a marine air-gun source (e.g., Jensen et al., 2011; Kennett & Fichtner, 2020). The input bubble pulse source at some depth below the sea surface can be approximated by a monopole, but the "ghost" reflection from the sea surface can create an image source with opposite phase, resulting in a wavefield radiated as if a dipole (the equivalent source) had been placed at the source. An example of an effective dipole for a volcanic source is a steep vent wall on one side of the source region that causes interaction of the acoustic waves with the solid topography boundary, such as that at Tungurahua volcano, Ecuador (Kim et al., 2012). Therefore, a stable dipole solution through time from multipole source inversions may be the result of true source directionality, not accounting for the effect of topography due to the use of 1-D Green's functions (e.g., De Angelis et al., 2016; Kim et al., 2012), or a combination of both. We note that even when studies attempt to account for the effects of topography, inaccuracies in the topography model used may still be present that limit the accuracy of the 3-D Green's functions. 3-D Green's functions that account for the effects of topography (and atmospheric conditions) allow for source inversions to yield a better characterization of the acoustic source (Diaz-Moreno et al., 2019; Fee et al., 2017; Iezzi et al., 2019; Kim et al., 2015, 2018; Kim & Rodgers, 2016).

One approach to validate the mass flow rate solutions for monopole inversions is to compare the solution to independent measures of eruption mass via multidisciplinary data (e.g., Fee et al., 2017). Another way to validate the solutions is to perform a synthetic investigation to determine the ability to resolve the source time function for a given scenario (e.g., Bean et al., 2008; Kim et al., 2012). We focus on the latter method to validate inversion solutions in this study.

1.4. Study Overview

Infrasound waveform inversions for the monopole source have been applied to short duration, impulsive explosions and have been shown to provide reasonable agreement with independent measures of mass flow rate for Vulcanian explosions of Sakurajima volcano, Japan (e.g., Fee et al., 2017), suggesting the monopole source may be an adequate approximation for simple explosion sources. However, the cautions and limitations of applying these methods to more complex, potentially directional sources (e.g., Diaz-Moreno et al., 2019; Iezzi et al., 2019) and their ability to resolve a unique and stable solution have not yet been investigated in detail. Kim et al. (2012) investigated the stability for multipole inversion in a half space, but did not use 3-D Green's functions.

Because infrasound source inversion methods are being developed and applied to more complex sources, the aim of this study is to explore situations when infrasound inversion methods may yield acceptable solutions, and when limitations should exist in trusting the retrieved solution. In this study, we perform infrasound waveform inversions for simple scenarios across a flat plane (i.e., no topography) as well as those that use 3-D Green's functions to account for the effects of topography for a variety of idealized and realistic deployment scenarios using Yasur volcano, Vanuatu as an example. We systematically vary the number and configuration of stations, degree of directionality, source frequency, noise level, and atmospheric conditions to investigate their impact on the results of the multipole infrasound waveform inversions. We emphasize that the main goals of this study are (a) the ability to recover the input source time functions for a given scenario and (b) to better understand the limitations of our inversions based on the network. This type of study may support infrasound station deployment decisions for both monitoring and research purposes and guide future infrasound deployments with a purpose of performing infrasound waveform inversions.

2. Methods

Here we describe the methods used for the waveform modeling to create 3-D Green's functions and subsequent multipole infrasound source inversion procedure. We investigate a few scenarios that use a flat plane (i.e., no topography) as well as focus on an example of Yasur volcano, Vanuatu for this synthetic study. Yasur is a 361 m tall volcano in the Vanuatu archipelago that has two sub-craters separated by a crater wall, making the influence of topography on infrasound propagation notable. While infrasound source inversion methods discussed here have been applied to both anthropogenic (e.g., Kim et al., 2018, 2020; Kim & Rodgers, 2016) and volcanic explosions (e.g., Diaz-Moreno et al., 2019; Fee et al., 2017; Iezzi et al., 2019; Kim et al., 2015), we chose to use an idealized volcanic explosion represented by a Blackman-Harris window function as the example source in this study, as volcanic topography and potential source time functions are likely more complex. We note that for this type of study, the input source characteristics and choice of topographic variability (as represented by a digital elevation model, DEM) are significantly less important than our ability to recover the input source time functions for a given network geometry.

The acoustic pressure $p(\mathbf{x_r}, t)$ at location $\mathbf{x_r}$ and time t can be represented by a monopole (mass flow rate) and the x, y, and z components of a dipole force given by Pierce (1989)

$$p(\mathbf{x_r}, t) = G(\mathbf{x_r}, t; \mathbf{x_s}) * \frac{\partial S(t)}{\partial t} + \frac{\partial G(\mathbf{x_r}, t; \mathbf{x_s})}{\partial x_s} * F_x(t) + \frac{\partial G(\mathbf{x_r}, t; \mathbf{x_s})}{\partial y_s} * F_y(t) + \frac{\partial G(\mathbf{x_r}, t; \mathbf{x_s})}{\partial z_s} * F_z(t) \quad (1)$$

where $G(\mathbf{x_r}, t; \mathbf{x_s})$ is the Green's function for a monopole, and $\mathbf{x_r}$ and $\mathbf{x_s}$ are the receiver and source position, respectively. Here, $S(t)$ is the mass flow rate at the source [kg/s], and $F_x(t)$, $F_y(t)$, and $F_z(t)$ are the time histories of forces in x, y, and z directions, respectively [kg m/s^2 = N]. $\partial/\partial x_s$, $\partial/\partial y_s$, and $\partial/\partial z_s$ denote partial derivatives with respect to the source coordinate.

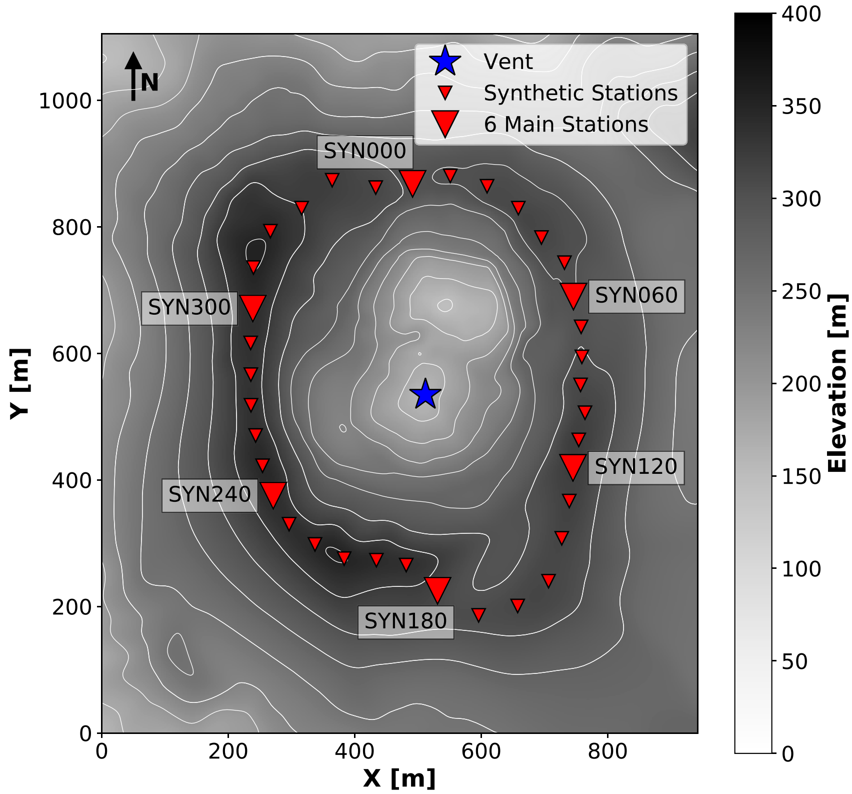

Figure 2. Map of Yasur volcano, Vanuatu showing the vent location (blue star) and synthetic stations (inverted red triangles) used in this study. The six stations for the default station configuration (SYN000, SYN060, SYN120, SYN180, SYN240, and SYN300) are shown as larger inverted triangles. The elevation contour interval is 25 m.

2.1. Waveform Modeling

The 3-D Green's functions that model realistic topography via a DEM are computed using the numerical approximation finite-difference time-domain (FDTD) modeling method of Kim and Lees (2014). This method treats topography as a rigid boundary and uses the Perfectly Matched Layers technique at the other model boundaries to remove reflections. We use both a flat plane as well as the DEM of Iezzi et al. (2019), which has a resolution of ~2 m in the crater region of Yasur. This DEM is re-sampled to a grid spacing of 2 m (*dh*) and trimmed to dimensions of 2.2 × 2 km and 0.75 km high surrounding the volcanic crater as preparation for the FDTD modeling procedure. This corresponds to 34 numerical grid nodes per shortest wavelength (68 m, or 5 Hz), which is greater than the recommended 10 grid nodes (Wang, 1996). We use a time step (*dt*) of 0.001 s, which satisfies the Courant condition for stability ($dt \leq dh/c\sqrt{3} = 0.0034$ s, with sound speed $c \approx 340$ m/s) and simulate for a duration of 6.0 s. For all results except for those in Section 3.4.3, a static sound speed profile above the source is used, therefore ignoring the impact of wind.

Monopole Green's functions are computed using a 5 Hz Blackman-Harris window function as the synthetic source placed at ground surface at the location of the vent (Vent A in Iezzi et al., 2019), the lowest point in the DEM in the southern crater (Figure 2). FDTD modeling outputs a pressure time history response to the Blackman-Harris window function source at a given station, which we refer to as the Green's functions, similar to previous studies (e.g., Fee et al., 2017; Iezzi et al., 2019; Kim et al., 2015). Synthetic receivers are located every 10° in azimuth on the surface of the crater rim, ranging from ~250–360 m horizontal distance from the synthetic source (Figure 2). These receivers are referred to as "SYNXXX," where XXX corresponds to the azimuth of the station relative to North (0°). A subset of these potential synthetic receivers are chosen for each of the source inversions performed. For the waveform modeling across a flat plane, synthetic stations are placed at the same X/Y locations as the topography example, with both the source and synthetic stations placed on the surface of the plane.

Two monopoles that are out of phase by 180° converge to a dipole, and the wavefield generated by the dipole can be mathematically expressed by a spatial derivative of the monopole Green's function. This is shown in Equation 1, where the acoustic response of the system to an arbitrary dipole, F_x, F_y, and F_z , is the spatial derivative of the monopole Green's function. We refer the reader to Morse and Ingard (1986) for more information, as well as Equation 8 with associated text of Kim et al. (2012) for formal derivation of Equation 1 and discussion about it. Our FDTD modeling procedure uses a staggered grid scheme (Ostashev et al., 2005) to compute the pressure and particle velocity separated by half grid intervals ($0.5dh$). The monopole and dipole sources cannot be placed at the exact same location and are instead displaced by a half grid interval ($0.5dh$). However, inverting for the multipole source (monopole and dipole sources simultaneously) assumes that the sources are co-located. Therefore, we numerically approximate the spatial derivative of the monopole Green's functions by using the central finite-difference differentiation in order to simulate the dipole source at the exact location as the monopole source. We refer to these spatial derivatives of the monopole Green's functions as the dipole Green's functions in this manuscript for simplicity.

2.2. Waveform Inversion

Synthetic waveforms are created from the linear combination of monopole and F_x, F_y, and F_z dipole Green's functions at a given synthetic receiver, downsampled to reflect a sampling frequency of 100 Hz ($dt = 0.01$ s). While some of our inversions use all four Green's functions, some use a subset of the components. For inversions in Section 3.4.1 where noise is added to the data, realistic noise is taken from data located on the crater rim similar to those in this study during a temporary deployment at Yasur volcano in 2016 (Iezzi et al., 2019; Jolly et al., 2017) for time periods when an explosion signal was not present in the data. These noise time series were bandpass filtered between 0.1 and 10 Hz, amplitudes scaled relative to the maximum pressure of each synthetic data waveform by the specified signal-to-noise ratio (SNR), and added to the synthetic waveforms prior to inversion.

We perform linearized acoustic waveform inversions for the monopole and multipole source vectors using the methods of Kim et al. (2015) and Iezzi et al. (2019), respectively, with a fixed source location. For all inversions except those in Section 3.4.3, no time shift between the synthetic data and Green's functions is allowed in the inversion procedure, a parameter that is sometimes used in order to account for unresolved factors that can affect arrival time. Similar to the synthetic waveform generation, some inversions solve for all four source time functions while others compute only a subset of the source terms. Equation 1 can be re-written as follows

$$\begin{bmatrix} \mathbf{g} & \mathbf{D_x} & \mathbf{D_y} & \mathbf{D_z} \end{bmatrix} \begin{bmatrix} \dot{S} \\ F_x \\ F_y \\ F_z \end{bmatrix} = \mathbf{Gm} = \mathbf{d} \quad (2)$$

where $\mathbf{d}$ is the $m \times 1$ data vector of synthetic waveforms (m = number of points in the data vector), $\mathbf{m}$ is the $4n \times 1$ solution vector of the mass flow rate and forces (n = number of point in the solution vector), and $\mathbf{g}$, $\mathbf{D_x}$, $\mathbf{D_y}$, and $\mathbf{D_z}$ are the $m \times n$ matrices representing the monopole (G) and dipole ($\partial G/\partial x_s$, $\partial G/\partial y_s$, $\partial G/\partial z_s$) Green's functions calculated from the FDTD forward model. Since $\mathbf{G}$ is an $m \times 4n$ matrix (compared with the $m \times 3n$ matrix in Kim et al., 2012) and m must be larger than $4n$ to avoid an under-determined problem, at least four stations should be used in order to uniquely determine the multipole solution with all four source components.

The solution $\mathbf{m}$ is solved for by minimizing the waveform misfit (R, residual) defined as

$$R = \frac{(\mathbf{d} - \mathbf{Gm})^T (\mathbf{d} - \mathbf{Gm})}{\mathbf{d}^T \mathbf{d}} \quad (3)$$

The residual is calculated using the iterative solver algorithm LSQR (Paige & Saunders, 1982) for the entire waveform for all stations used in the inversion. The residual ranges from 0 to 1, where a residual of 0 represents the model fitting 100% of the data. The inversion procedure produces the expected infrasound waveform (in Pa) for each synthetic receiver used in the inversion as well as the solution vectors, which include a subset of the mass flow rate ($S(t)$ in kg/s) and force components (F_x, F_y, and F_z in N). The reader is referred to Kim et al. (2012, 2015), and Iezzi et al. (2019) for additional details on the source inversion method.

3. Inversion Solution Investigation

In this section, we systematically vary the number and configuration of stations, dipole strength (square root of the sum of the squares of each of the three force components) relative to the monopole, source frequency, signal-to-noise ratio (SNR), iterative solver parameters, and atmospheric conditions (winds) and investigate their impact on the results of the infrasound waveform inversions. The first set of inversions in Sections 3.1 and 3.2 consider propagation across a flat plane, while Sections 3.1 and 3.3–3.5 use 3-D Green's functions created using Yasur volcano, Vanuatu as the example DEM. For each scenario, we state the type of data used in the inversion (i.e., the input source) and the type of source we allow in the inversion. The output solution vectors ("inversion solution") are compared with the input solution vectors ("true solution") to determine how well each inversion scenario is able to resolve the unique input solution. For Sections 3.1–3.3, the synthetic data are a replica of the linear combination of the 3-D Green's functions components (monopole, F_x, F_y, F_z), but realistic parameters such as noise are added to the synthetic data in Sections 3.4 and 3.5. Unless otherwise specified, the default specifications used in the following inversions are: (a) an "average station deployment" of 6 ground stations placed on the crater rim with equal azimuthal spacing (SYN000, SYN060, SYN120, SYN180, SYN240, and SYN300; large inverted triangles in Figure 2); (b) a dipole orientation for multipole inversions of F_x, F_y, and $F_z = (1, 1, 1)$ that we refer to as the "slanted dipole," which yields a force pointing up and to the northeast (45° azimuth and ~35° inclination); (c) inversions that include noise added to the data default to a SNR of 10; and (d) iterative solver parameters of residual tolerance of 0.01 over 10 iterations, with a maximum number of iterations determined by the length of the data vector multiplied by the length of the solution vector. The parameters used for each inversion scenario are summarized in Table 1.

3.1. Comparison of Inversion Types

We begin our investigation by comparing infrasound waveform inversions for the monopole only, monopole and single force, and multipole sources, using Green's functions from simulations across a flat plane as well as inversions that use Yasur topography. The inversions performed are: (a) Monopole data, Monopole inversion (Figure 3a), (b) Monopole + F_x data, Monopole + F_x inversion (Figures 3b and 3c), (c) Monopole + F_y data, Monopole + F_y inversion (Figures 3d and 3e), (d) Monopole + F_z (monopole + vertical dipole) data, Monopole + F_z (monopole + vertical dipole) inversion (Figures 3f and 3g), and (e) Monopole + F_x + F_y + F_z (monopole + slanted dipole) data, Monopole + F_x + F_y + F_z (monopole + slanted dipole) inversion (Figures 3h–3k). We find that the mass flow rate can be recovered in all cases investigated, both with and without topography (Figures 3a, 3b, 3d, 3f and 3h). For the monopole + vertical dipole and monopole + slanted dipole inversions without topography, the F_z component is not recovered at all because the sensors are on the plane where there is no radiation resulting from the vertical dipole. The inclusion of topography (and therefore sensors above the source) increases the amplitude of the F_z component recovered, but the network distribution cannot recover the true solution.

3.2. Simple Inversions: No Topography

We next focus on simple source inversions that use Green's functions that were created by propagation over a flat plane, meaning no topography is considered. These inversions can give insight into the impact of multipole sources on inversion results, but likely are not realistic for many deployment environments where topography is pronounced (e.g., volcanoes).

3.2.1. Single Station Monopole Inversions

In the simplest deployment scenario, a single infrasound sensor can be used to invert for the monopole source if the source location is known. We perform 36 separate monopole inversions, each with a single station placed every 10° in azimuth surrounding the source. Synthetic data are created by a multipole source (monopole + slanted dipole) with the dipole source amplitudes multiplied by 10 (termed "dipole scale") relative to the monopole source with peak mass flow rate of 1 kg/s. We first investigate the monopole and slanted dipole Green's functions

Table 1
Parameters for Each Inversion Scenario

Source type	Data type	Topo	# of stations	Source freq	Dipole scale	SNR	Iteration settings	Wind	Figures	Main result
Monopole	Monopole	*n*	6	5	–	–	default	–	3a	Mass flow rate, Fx, and Fy solutions recovered; Fz component is not recovered at all
Monopole + Fx	Monopole + Fx	*n*	6	5	1	–	default	–	3b and 3c	
Monopole + Fy	Monopole + Fy	*n*	6	5	1	–	default	–	3d and 3e	
Monopole + Fz	Monopole + Fz	*n*	6	5	1	–	default	–	3f and 3g	
Monopole + Fx + Fy + Fz	Monopole + Fx + Fy + Fz	*n*	6	5	1	–	default	–	3h–3k	
Monopole	Monopole	*y*	6	5	–	–	default	–	3a/12	Mass flow rate, Fx, and Fy solutions recovered; Fz component is partially recovered
Monopole + Fx	Monopole + Fx	*y*	6	5	1	–	default	–	3b and 3c	
Monopole + Fy	Monopole + Fy	*y*	6	5	1	–	default	–	3d and 3e	
Monopole + Fz	Monopole + Fz	*y*	6	5	1	–	default	–	3f and 3g	
Monopole + Fx + Fy + Fz	Monopole + Fx + Fy + Fz	*y*	6	5	1	–	default	–	3h–3k	
Monopole	Monopole + Fx + Fy + Fz	*n*	1	5	10	–	default	–	4	Mass flow rate solution is dependent on the azimuth at which the station is placed relative to the dipole azimuth
Monopole	Monopole + Fz	*n*	6	5	1	–	default	–	5a, 5c and 5d	Mass flow rate solution is well recovered and residual is nearly zero for all dipole strengths
Monopole	Monopole + Fz	*n*	6	5	5	–	default	–	5a, 5c and 5d	
Monopole	Monopole + Fz	*n*	6	5	10	–	default	–	5a, 5c and 5d	
Monopole	Monopole + Fz	*n*	6	5	15	–	default	–	5a, 5c and 5d	
Monopole	Monopole + Fz	*n*	6	5	20	–	default	–	5a, 5c and 5d	
Monopole	Monopole + Fx + Fy + Fz	*n*	6	5	1	–	default	–	5b, 5c and 5d	Mass flow rate is well-recovered, but the residual increases for increasing dipole strength
Monopole	Monopole + Fx + Fy + Fz	*n*	6	5	5	–	default	–	5b, 5c and 5d	
Monopole	Monopole + Fx + Fy + Fz	*n*	6	5	10	–	default	–	5b, 5c and 5d	
Monopole	Monopole + Fx + Fy + Fz	*n*	6	5	15	–	default	–	5b, 5c and 5d	
Monopole	Monopole + Fx + Fy + Fz	*n*	6	5	20	–	default	–	5b, 5c and 5d	
Monopole	Monopole + Fz	*n*	6 (east)	5	1	–	default	–	5e, 5g and 5h	Mass flow rate solution is well recovered and residual is nearly zero for all dipole strengths
Monopole	Monopole + Fz	*n*	6 (east)	5	5	–	default	–	5e, 5g and 5h	
Monopole	Monopole + Fz	*n*	6 (east)	5	10	–	default	–	5e, 5g and 5h	
Monopole	Monopole + Fz	*n*	6 (east)	5	15	–	default	–	5e, 5g and 5h	
Monopole	Monopole + Fz	*n*	6 (east)	5	20	–	default	–	5e, 5g and 5h	
Monopole	Monopole + Fx + Fy + Fz	*n*	6 (east)	5	1	–	default	–	5f, 5g and 5h	Non-symmetrical network geometries can yield larger percent underestimations of the peak mass flow rate than a symmetrical network
Monopole	Monopole + Fx + Fy + Fz	*n*	6 (east)	5	5	–	default	–	5f, 5g and 5h	
Monopole	Monopole + Fx + Fy + Fz	*n*	6 (east)	5	10	–	default	–	5f, 5g and 5h	
Monopole	Monopole + Fx + Fy + Fz	*n*	6 (east)	5	15	–	default	–	5f, 5g and 5h	
Monopole	Monopole + Fx + Fy + Fz	*n*	6 (east)	5	20	–	default	–	5f, 5g and 5h	

Table 1
Continued

Source type	Data type	Topo	# of stations	Source freq	Dipole scale	SNR	Iteration settings	Wind	Figures	Main result
Monopole	Monopole + Fz	*y*	6	5	1	–	default	–	6a, 6c and 6d/ 7e, 7i and 7j	Peak mass flow rate of the inversion solution decreases and waveform residual increases for increasing dipole strength
Monopole	Monopole + Fz	*y*	6	5	5	–	default	–	6a, 6c and 6d/ 7e, 7i and 7j	
Monopole	Monopole + Fz	*y*	6	5	10	–	default	–	6a, 6c and 6d/ 7e, 7i and 7j/ 9a–9d	
Monopole	Monopole + Fz	*y*	6	5	15	–	default	–	6a, 6c and 6d/ 7e, 7i and 7j	
Monopole	Monopole + Fz	*y*	6	5	20	–	default	–	6a, 6c and 6d/ 7e, 7i and 7j	
Monopole	Monopole + Fx + Fy + Fz	*y*	6	5	1	–	default	–	6b, 6c and 6d/ 7f, 7i and 7j	Peak mass flow rate of the inversion solution decreases (more slowly compared to the monopole and vertical only dipole case) and waveform residual increases for increasing dipole strength
Monopole	Monopole + Fx + Fy + Fz	*y*	6	5	5	–	default	–	6b, 6c and 6d/ 7f, 7i and 7j	
Monopole	Monopole + Fx + Fy + Fz	*y*	6	5	10	–	default	–	6b, 6c and 6d/ 7f, 7i and 7j	
Monopole	Monopole + Fx + Fy + Fz	*y*	6	5	15	–	default	–	6b, 6c and 6d/ 7f, 7i and 7j	
Monopole	Monopole + Fx + Fy + Fz	*y*	6	5	20	–	default	–	6b, 6c and 6d/ 7f, 7i and 7j	
Monopole	Monopole + Fz	*y*	6	5	1	10	default	–	6c and 6d	Lower percent underestimation of peak mass flow rate inversion solution for all data types and dipole strengths investigated compared with the no noise case; Inversions in which noise is added to the data result in higher residuals than the same inversion performed without noise
Monopole	Monopole + Fz	*y*	6	5	5	10	default	–	6c and 6d	
Monopole	Monopole + Fz	*y*	6	5	10	10	default	–	6c and 6d	
Monopole	Monopole + Fz	*y*	6	5	15	10	default	–	6c and 6d	
Monopole	Monopole + Fz	*y*	6	5	20	10	default	–	6c and 6d	
Monopole	Monopole + Fx + Fy + Fz	*y*	6	5	1	10	default	–	6c and 6d	
Monopole	Monopole + Fx + Fy + Fz	*y*	6	5	5	10	default	–	6c and 6d	
Monopole	Monopole + Fx + Fy + Fz	*y*	6	5	10	10	default	–	6c and 6d	
Monopole	Monopole + Fx + Fy + Fz	*y*	6	5	15	10	default	–	6c and 6d	
Monopole	Monopole + Fx + Fy + Fz	*y*	6	5	20	10	default	–	6c and 6d	

Table 1
Continued

Source type	Data type	Topo	# of stations	Source freq	Dipole scale	SNR	Iteration settings	Wind	Figures	Main result
Monopole	Monopole + Fz	y	6	5	1	10 (Gaussian)	default	–	6c and 6d	Peak mass flow rate inversion solution and waveform residual for all data types and dipole strengths investigated similar to the no noise case
Monopole	Monopole + Fz	y	6	5	5	10 (Gaussian)	default	–	6c and 6d	
Monopole	Monopole + Fz	y	6	5	10	10 (Gaussian)	default	–	6c and 6d	
Monopole	Monopole + Fz	y	6	5	15	10 (Gaussian)	default	–	6c and 6d	
Monopole	Monopole + Fz	y	6	5	20	10 (Gaussian)	default	–	6c and 6d	
Monopole	Monopole + Fx + Fy + Fz	y	6	5	1	10 (Gaussian)	default	–	6c and 6d	
Monopole	Monopole + Fx + Fy + Fz	y	6	5	5	10 (Gaussian)	default	–	6c and 6d	
Monopole	Monopole + Fx + Fy + Fz	y	6	5	10	10 (Gaussian)	default	–	6c and 6d	
Monopole	Monopole + Fx + Fy + Fz	y	6	5	15	10 (Gaussian)	default	–	6c and 6d	
Monopole	Monopole + Fx + Fy + Fz	y	6	5	20	10 (Gaussian)	default	–	6c and 6d	
Monopole	Monopole + Fz	y	6	1	1	–	default	–	7a, 7i and 7j	Peak mass flow rate for the inversion solution decreases with increasing dipole strength
Monopole	Monopole + Fz	y	6	1	5	–	default	–	7a, 7i and 7j	
Monopole	Monopole + Fz	y	6	1	10	–	default	–	7a, 7i and 7j	
Monopole	Monopole + Fz	y	6	1	15	–	default	–	7a, 7i and 7j	
Monopole	Monopole + Fz	y	6	1	20	–	default	–	7a, 7i and 7j	
Monopole	Monopole + Fx + Fy + Fz	y	6	1	1	–	default	–	7b, 7i and 7j	Peak mass flow rate for the inversion solution decreases with increasing dipole strength but is less affected by the source frequency compared to the monopole and vertical only dipole case
Monopole	Monopole + Fx + Fy + Fz	y	6	1	5	–	default	–	7b, 7i and 7j	
Monopole	Monopole + Fx + Fy + Fz	y	6	1	10	–	default	–	7b, 7i and 7j	
Monopole	Monopole + Fx + Fy + Fz	y	6	1	15	–	default	–	7b, 7i and 7j	
Monopole	Monopole + Fx + Fy + Fz	y	6	1	20	–	default	–	7b, 7i and 7j	
Monopole	Monopole + Fz	y	6	3	1	–	default	–	7c, 7i and 7j	Peak mass flow rate for the inversion solution decreases with increasing dipole strength
Monopole	Monopole + Fz	y	6	3	5	–	default	–	7c, 7i and 7j	
Monopole	Monopole + Fz	y	6	3	10	–	default	–	7c, 7i and 7j	
Monopole	Monopole + Fz	y	6	3	15	–	default	–	7c, 7i and 7j	
Monopole	Monopole + Fz	y	6	3	20	–	default	–	7c, 7i and 7j	
Monopole	Monopole + Fx + Fy + Fz	y	6	3	1	–	default	–	7d, 7i and 7j	Peak mass flow rate for the inversion solution decreases with increasing dipole strength but is less affected by the source frequency compared to the monopole and vertical only dipole case
Monopole	Monopole + Fx + Fy + Fz	y	6	3	5	–	default	–	7d, 7i and 7j	
Monopole	Monopole + Fx + Fy + Fz	y	6	3	10	–	default	–	7d, 7i and 7j	
Monopole	Monopole + Fx + Fy + Fz	y	6	3	15	–	default	–	7d, 7i and 7j	
Monopole	Monopole + Fx + Fy + Fz	y	6	3	20	–	default	–	7d, 7i and 7j	

Table 1
Continued

Source type	Data type	Topo	# of stations	Source freq	Dipole scale	SNR	Iteration settings	Wind	Figures	Main result
Monopole	Monopole + Fz	*y*	6	7	1	–	default	–	7g, 7i and 7j	Peak mass flow rate for the inversion solution decreases with increasing source frequency, which is likely due to increased sampling per period
Monopole	Monopole + Fz	*y*	6	7	5	–	default	–	7g, 7i and 7j	
Monopole	Monopole + Fz	*y*	6	7	10	–	default	–	7g, 7i and 7j	
Monopole	Monopole + Fz	*y*	6	7	15	–	default	–	7g, 7i and 7j	
Monopole	Monopole + Fz	*y*	6	7	20	–	default	–	7g, 7i and 7j	
Monopole	Monopole + Fx + Fy + Fz	*y*	6	7	1	–	default	–	7h, 7i and 7j	Peak mass flow rate for the inversion solution decreases with increasing source frequency and is less affected by the source frequency compared to the monopole and vertical only dipole case
Monopole	Monopole + Fx + Fy + Fz	*y*	6	7	5	–	default	–	7h, 7i and 7j	
Monopole	Monopole + Fx + Fy + Fz	*y*	6	7	10	–	default	–	7h, 7i and 7j	
Monopole	Monopole + Fx + Fy + Fz	*y*	6	7	15	–	default	–	7h, 7i and 7j	
Monopole	Monopole + Fx + Fy + Fz	*y*	6	7	20	–	default	–	7h, 7i and 7j	
Monopole + Fx + Fy	Monopole + Fx + Fy + Fz	*y*	6	5	1	–	default	–	8	Amplitude and exact direction of the dipole may not be correct if there is a substantial vertical dipole (Fz) component
Monopole + Fx + Fy + Fz	Monopole + Fx + Fy + Fz	*y*	3	5	1	–	default	–	9a–9d	Mass flow rate solution vector can be resolved regardless of the number of stations around the source; Vertical dipole solution is not resolved even with 12 stations
Monopole + Fx + Fy + Fz	Monopole + Fx + Fy + Fz	*y*	6	5	1	–	default	–	9a–9j	
Monopole + Fx + Fy + Fz	Monopole + Fx + Fy + Fz	*y*	12	5	1	–	default	–	9a–9d	
Monopole	Monopole	*y*	6	5	–	2	default	–	10a	Inversions that include data with a SNR of 5 or greater produce reasonable source solutions
Monopole	Monopole	*y*	6	5	–	5	default	–	10a	
Monopole	Monopole	*y*	6	5	–	10	default	–	10a	
Monopole	Monopole	*y*	6	5	–	20	default	–	10a	
Monopole + Fx + Fy + Fz	Monopole + Fx + Fy + Fz	*y*	6	5	10	2	default	–	10b–10e	Inversions that include data with a SNR of 5 or greater produce reasonable source solutions, with the exception of the vertical dipole component
Monopole + Fx + Fy + Fz	Monopole + Fx + Fy + Fz	*y*	6	5	10	5	default	–	10b–10e	
Monopole + Fx + Fy + Fz	Monopole + Fx + Fy + Fz	*Y*	6	5	10	10	default	–	10b–10e/13	
Monopole + Fx + Fy + Fz	Monopole + Fx + Fy + Fz	*Y*	6	5	10	20	default	–	10b–10e	
Monopole	Monopole	*Y*	6	5	–	10	5	–	11a and 11f	Inversion solution is very similar to the true solution regardless of the number of iterations performed (greater than 5 iterations)
Monopole	Monopole	*Y*	6	5	–	10	10	–	11a and 11f	
Monopole	Monopole	*Y*	6	5	–	10	50	–	11a and 11f	
Monopole	Monopole	*Y*	6	5	–	10	100	–	11a and 11f	
Monopole	Monopole	*Y*	6	5	–	10	500	–	11a and 11f	
Monopole	Monopole	*Y*	6	5	–	10	1000	–	11a and 11f	
Monopole	Monopole	*Y*	6	5	–	10	5000	–	11a and 11f	

Table 1
Continued

Source type	Data type	Topo	# of stations	Source freq	Dipole scale	SNR	Iteration settings	Wind	Figures	Main result
Monopole + Fx + Fy + Fz	Monopole + Fx + Fy + Fz	Y	6	5	10	10	5	–	11b–11g	For iteration numbers between 5 and 100, the true source is resolved fairly well for all four source components; however, for iterations 500 and greater, "spurious forces" exist in all four components 0.5 s after the explosion onset
Monopole + Fx + Fy + Fz	Monopole + Fx + Fy + Fz	Y	6	5	10	10	10	–	11b–11g	
Monopole + Fx + Fy + Fz	Monopole + Fx + Fy + Fz	Y	6	5	10	10	50	–	11b–11g	
Monopole + Fx + Fy + Fz	Monopole + Fx + Fy + Fz	Y	6	5	10	10	100	–	11b–11g	
Monopole + Fx + Fy + Fz	Monopole + Fx + Fy + Fz	Y	6	5	10	10	500	–	11b–11g	
Monopole + Fx + Fy + Fz	Monopole + Fx + Fy + Fz	Y	6	5	10	10	1000	–	11b–11g	
Monopole + Fx + Fy + Fz	Monopole + Fx + Fy + Fz	Y	6	5	10	10	5000	–	11b–11g	
Monopole	Monopole	Y	6	5	–	–	default	10	12	An appropriate xcor value allows for the waveforms to line up properly, lowers the waveform residual to 0.01 from 0.20, and is able to resolve the massflow rate solution well

Note. The table shows the source type inverted for, the data type used in the inversion, whether or not topography was accounted for, the number of stations, source frequency, dipole scale factor relative to the monopole, signal to noise ratio (SNR) added to the data prior to inversion, iterative solver settings, wind, corresponding figures, and the main result from each set of inversions.

at two stations, SYN040 (Figure 4a) located to the northeast and SYN220 (Figure 4b) located to the southwest, in detail. In these two examples, the addition of the slanted dipole Green's functions (dotted line) to the monopole Green's function (dashed line) to create the synthetic data (solid line) results in the peak of the resulting data vector being slightly shifted from that of the monopole Green's function alone. When solving for a monopole source when the true source is a multipole, this results in a shift of the peak mass flow rate of the inversion solutions for these two examples, as shown in Figure 4c, relative to the true input solution and both inversions result in an overestimation of the true peak mass flow rate. The inversion solution for each of the 36 inversions is shown in Figure 4d, where it can be seen that the solution is dependent on the azimuth at which the station is placed relative to the dipole azimuth (up and to the northeast, 45° azimuth and ~35° inclination). This is represented by the percent overestimation of the peak mass flow rate solution relative to the true input source (Figure 4e). For this scenario, the peak mass flow rate is overestimated by up to ~10% for inversions that use a station placed to the northeast and southwest azimuths. Additionally, we note that because only one station was used in each inversion, the waveform residual is zero for all inversions (Figure 4f).

3.2.2. Monopole Inversions With Varying Modeled Dipole Strength

We create synthetic data using a combination of monopole + vertical dipole data (i.e., no horizontal dipole components), as well as a set with monopole and all three dipole components (monopole + slanted dipole) using Green's functions across a flat plane but perform inversions for only the monopole source. The dipole scale (value by which the dipole amplitudes are multiplied) is varied between 1 and 20 times relative to the constant peak monopole mass flow rate of 1 kg/s for each inversion. The scenario with all three dipole components is scaled based on the dipole strength (square root of the sum of the squares of each of the three components) so that the dipole strength is the same as the results with the vertical dipole only case. Therefore, the dipole strength used to create the data is the same with respect to the monopole, whether only the F_z component or all three dipole components were used. We test two different deployment scenarios, the first being the default deployment of six stations evenly distributed around the source (Figures 5a–5d) and another with six stations that are located only on the eastern half of the source (azimuths of 0–180°, Figures 5e–5h).

When the stations are equally spaced around the source and there is no topography (Figures 5a–5d), the mass flow rate solution for both the monopole + vertical dipole data (Figure 5a) and monopole and all three dipole components (monopole + slanted dipole, Figure 5b) are nearly the true solution. This is quantified by plotting the percent underestimation of peak mass flow rate of the solution in Figure 5c. Figure 5d shows that the residual remains zero for the monopole + vertical dipole case, but increases for the monopole + slanted dipole with increasing dipole strength. However, if the sensors are not equally distributed and instead grouped on the East side of the source only (Figures 5e–5h), the mass flow rate solution for monopole inversions that use monopole + slanted dipole data begin to show differences (Figure 5g). The waveform residuals remain low (Figure 5h), which differs from the symmetrical network configuration case (Figure 5d).

3.3. Ideal Inversions: Noise Free

The next set of waveform inversions investigate ideal inversions using the topography of Yasur volcano that do not have the addition of realistic parameters such as noise or wind to the data. While these inversions are unrealistic for real data,

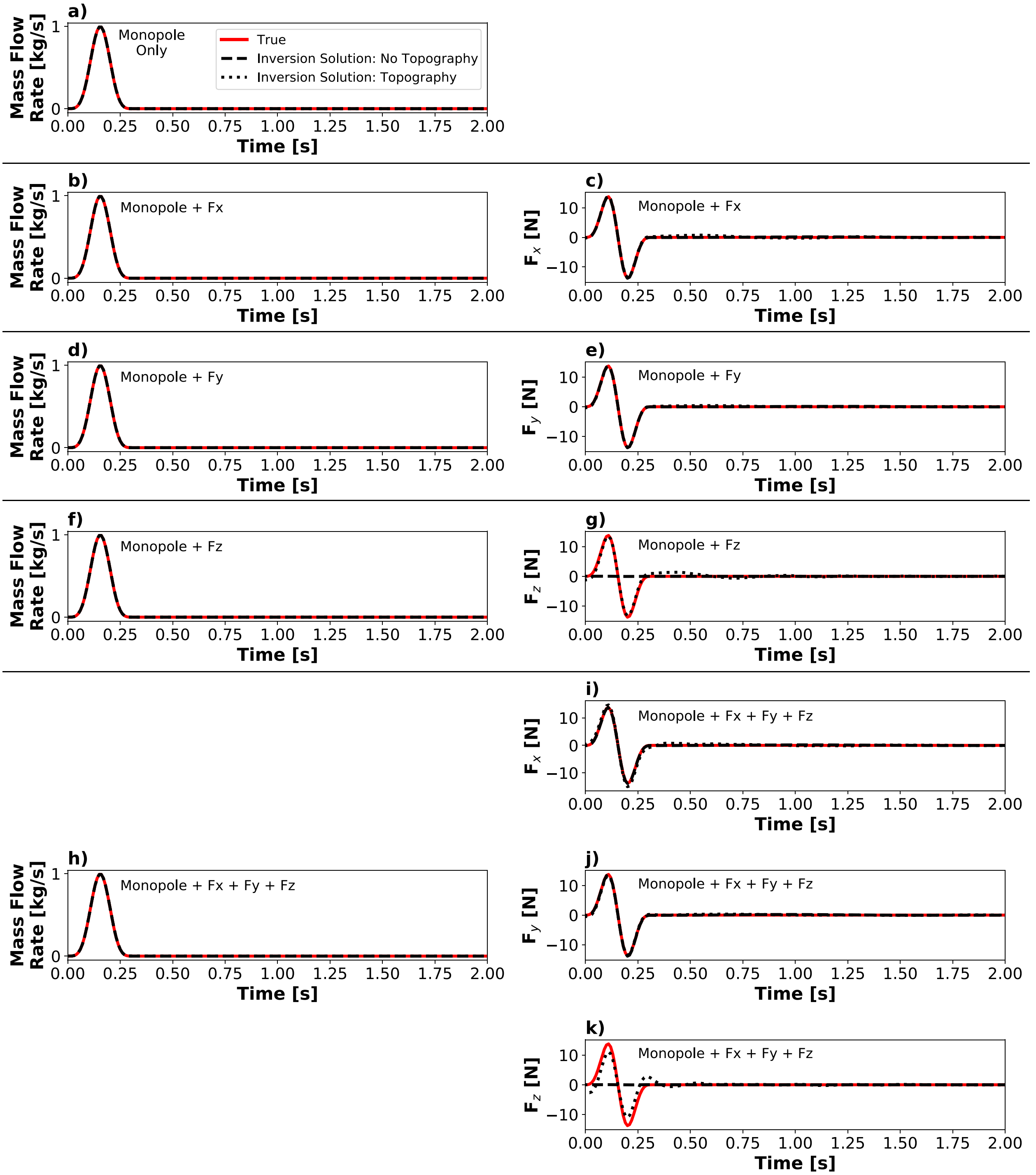

Figure 3. Monopole, Monopole + single force, and multipole inversions across a flat plane and topography. (a) Monopole-only, (b and c) Monopole + F_x, (d and e) Monopole + F_y, (f and g) Monopole + F_z (monopole + vertical dipole), and (h–k) Monopole + $F_x + F_y + F_z$ (monopole + slanted dipole) source inversions for six stations spread equally in azimuth. The true solution is shown in red and the recovered inversion solutions are shown in black dashed (no topography) and dotted (topography) lines.

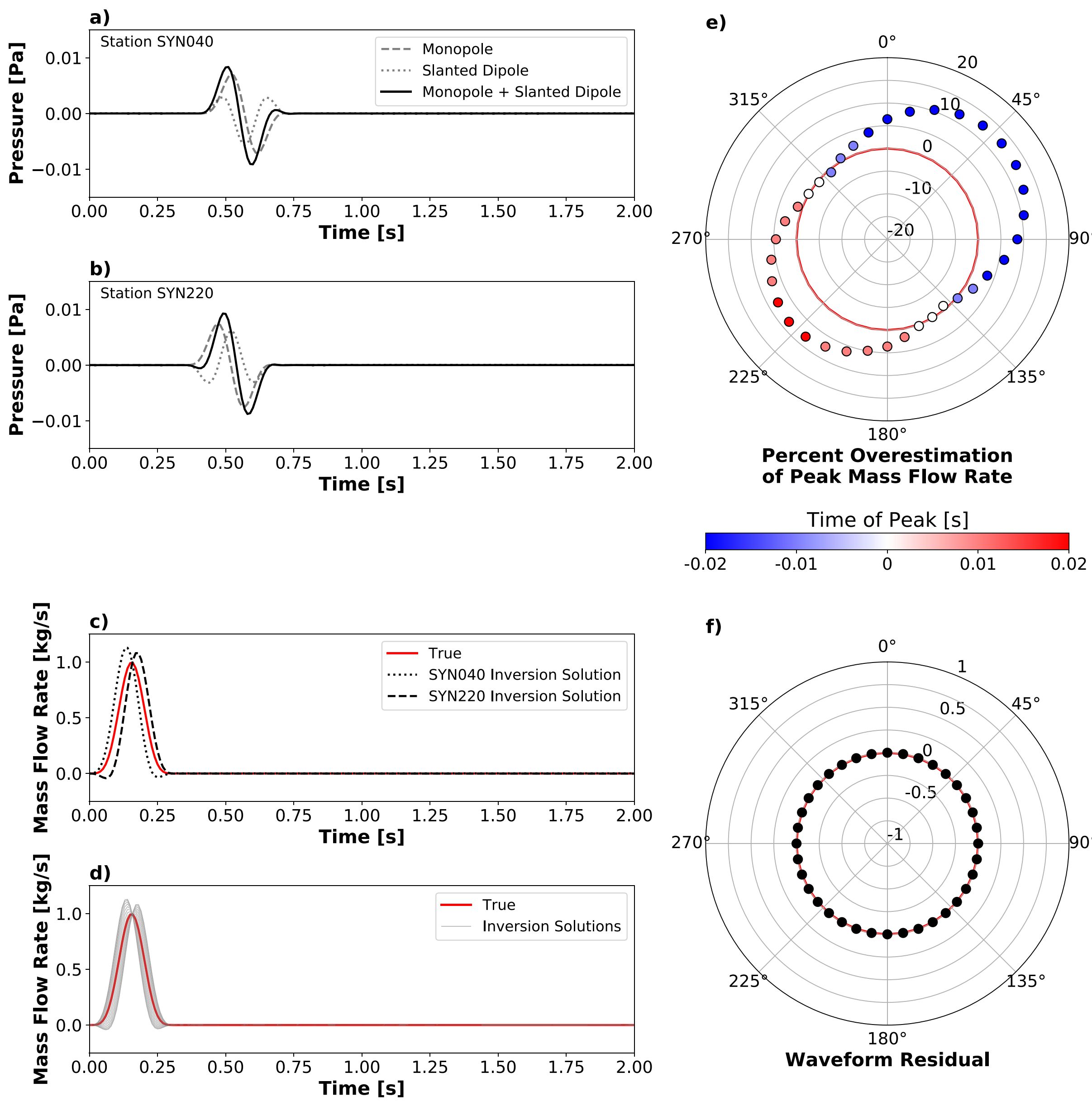

Figure 4. Single station monopole inversion with monopole + slanted dipole data across a flat plane. Monopole (dashed) and slanted dipole (dotted) Green's functions as well as the addition of the two to make synthetic data (solid line) for station (a) SYN040 (northeast) and (b) SYN220 (southwest). Monopole-only source inversions that use only a single station placed on the Yasur crater rim for (c) Stations SYN040 and SYN220 and (d) all 36 inversions each with a station placed every 10° in azimuth using multipole (monopole + slanted dipole) data for a dipole strength of 10. The true solution is shown in red and the recovered inversion solutions for each of the 36 inversions are shown in gray. (e) Percent overestimation of the peak mass flow rate colored by the time of the peak relative to the true solution and (f) waveform residual for each inversion.

they are a necessary step to determine if an inversion solution can be resolved even in the absence of noise, as noise will only decrease the ability to obtain the true inversion solution.

3.3.1. Monopole Inversions With Increasing Modeled Dipole Strength

Similar to Section 3.2.2 but now including the effects of topography, we create synthetic data using a combination of monopole and vertical dipole data (i.e., no horizontal dipole components) but perform inversions for only the monopole source. The dipole strength is varied between 1 and 20 times relative to the constant peak mass flow rate of 1 kg/s for each inversion. The resulting mass flow rate solution vectors for each of these inversions are shown in Figure 6a. Our results indicate that the overall shape of the mass flow rate solution is similar, but the

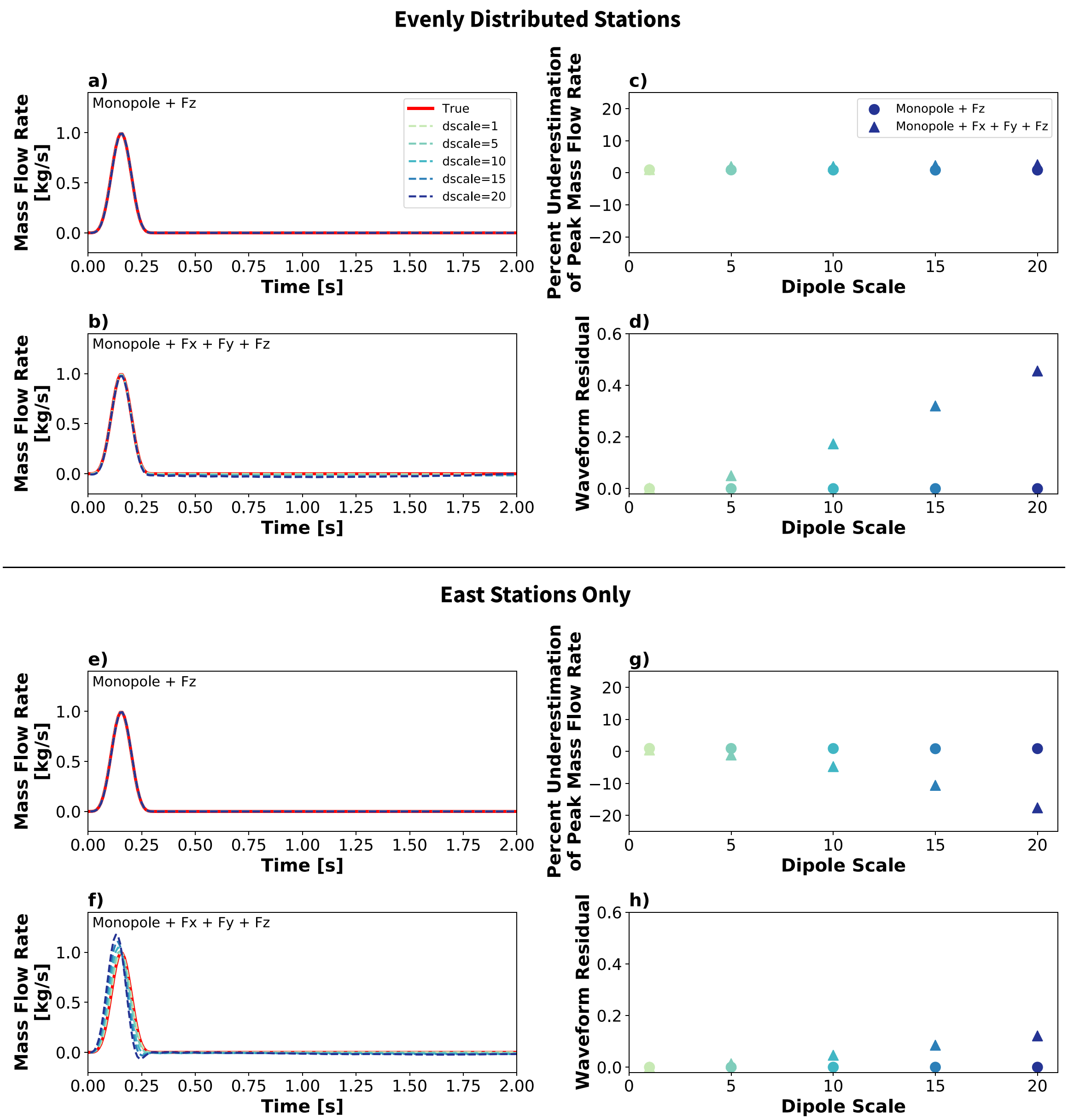

Figure 5. Inversion results for varying data dipole strength with simulations across a flat plane. Monopole-only source inversion for six stations placed (a–d) evenly distributed in azimuth and (e–h) only on the East half using (a and e) monopole + vertical dipole (monopole + F_z) and (b and f) monopole + slanted dipole (monopole + $F_x + F_y + F_z$) data for increasing dipole strengths relative to the monopole amplitude between 1 and 20. The true solution is shown in red and the recovered inversion solutions are shown using light to dark blue corresponding to increasing dipole scale relative to the monopole. (c and g) Percent underestimation of the peak mass flow rate and (d and h) waveform residual for each inversion.

peak mass flow rate of the inversion solution decreases for increasing relative dipole strength, where the highest dipole scale of 20 we tested can only recover up to 75% of the peak mass flow rate.

The aforementioned process is repeated for data that are created from a combination of monopole and all three dipole components (monopole + slanted dipole). The peak mass flow rate for the inversion solution again decreases with increasing dipole strength (Figure 6b), but decreases more slowly compared to the monopole and vertical only dipole case (Figure 6a). We quantify this using a calculation of the percent underestimation of the peak mass flow rate relative to the true peak mass flow rate (Figure 6c). The mass flow rate inversion solution for data created from the monopole and vertical-only dipole has a higher percent underestimation of the peak mass flow rate relative to the inversions where data are created using data created from the monopole and slanted dipole for the

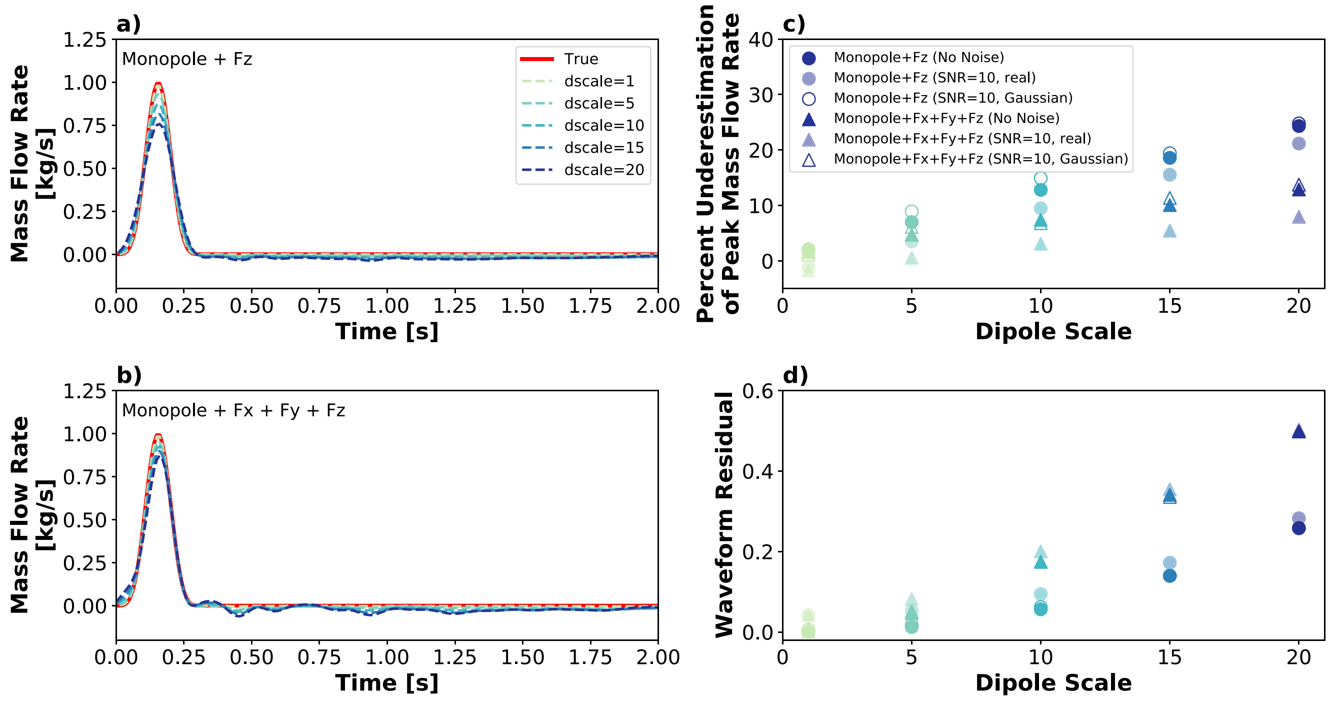

Figure 6. Inversion results for increasing data dipole strength with simulations across topography. Monopole-only source inversion for six stations placed on the Yasur crater rim spread equally in azimuth using (a) monopole + vertical dipole (monopole + F_z) and (b) monopole + slanted dipole (monopole + $F_x + F_y + F_z$) data for increasing dipole strengths relative to the monopole amplitude between 1 and 20. The true solution is shown in red and the recovered inversion solutions are shown using light to dark blue corresponding to increasing dipole scale relative to the monopole. (c) Percent underestimation of the peak mass flow rate and (d) waveform residual for each inversion, where solid markers show results for noise free inversions, light shaded markers show results with real noise added (SNR = 10), and open face markers show results with Gaussian noise added (SNR = 10).

same dipole strength (Figure 6c). We note that this may not necessarily equate to an improved or more accurate solution, as the "less underestimated" mass flow rate solution for the monopole and all three dipole components inversions (Figure 6b) may be due to the combined effect of underestimation by the F_z component (Figure 6a) and overestimation by F_x and F_y components (i.e., the effects may cancel each other out). As expected, the waveform residual increases with increasing relative dipole strength for both cases (Figure 6d). The residual is larger for inversions where data was created using the monopole and all three force components as compared to those using data created using monopole and F_z components for all dipole strengths. For data created using monopole and vertical only dipole force, the residual remains under 0.10 for scenarios in which dipole amplitudes are multiplied by less than 10 (~100 N compared with 1 kg/s).

3.3.2. Monopole Inversions for Varying Source Frequencies

Infrasound sources contain different dominant source frequencies, which may impact the ability to resolve the true source using acoustic waveform inversion techniques. We perform a similar procedure of monopole inversions to Section 3.3.1 using 1 Hz (Figures 7a and 7b), 3 Hz (Figures 7c and 7d), 5 Hz (Figures 7e and 7f), and 7 Hz (Figures 7g and 7h) sources using synthetic data created from a combination of monopole and vertical dipole data (i.e., no horizontal dipole components, Figures 7a, 7c, 7e and 7g) and a combination of monopole and all three dipole components (Figures 7b, 7d, 7f and 7h). For all frequencies, the peak mass flow rate for the inversion solution decreases with increasing dipole strength (Figures 7a–7h). For the inversions using a combination of monopole and vertical dipole data (Figures 7a, 7c, 7e and 7g) the peak mass flow rate for the inversion solution decreases with increasing source frequency, while the inversions using a combination of monopole and all three dipole components (Figures 7b, 7d, 7f and 7h) appear less affected by the source frequency for the station configuration used. This is shown by Figure 7i, where the percent underestimation of the peak mass flow rate solution is shown for each relative dipole strength value. The waveform residual increases with increasing source frequency for all dipole strengths (Figure 7j), consistent with results from Section 3.3.1. We note that the inversions in this section were all performed with the same *dt* to imitate having a consistent sampling frequency despite the

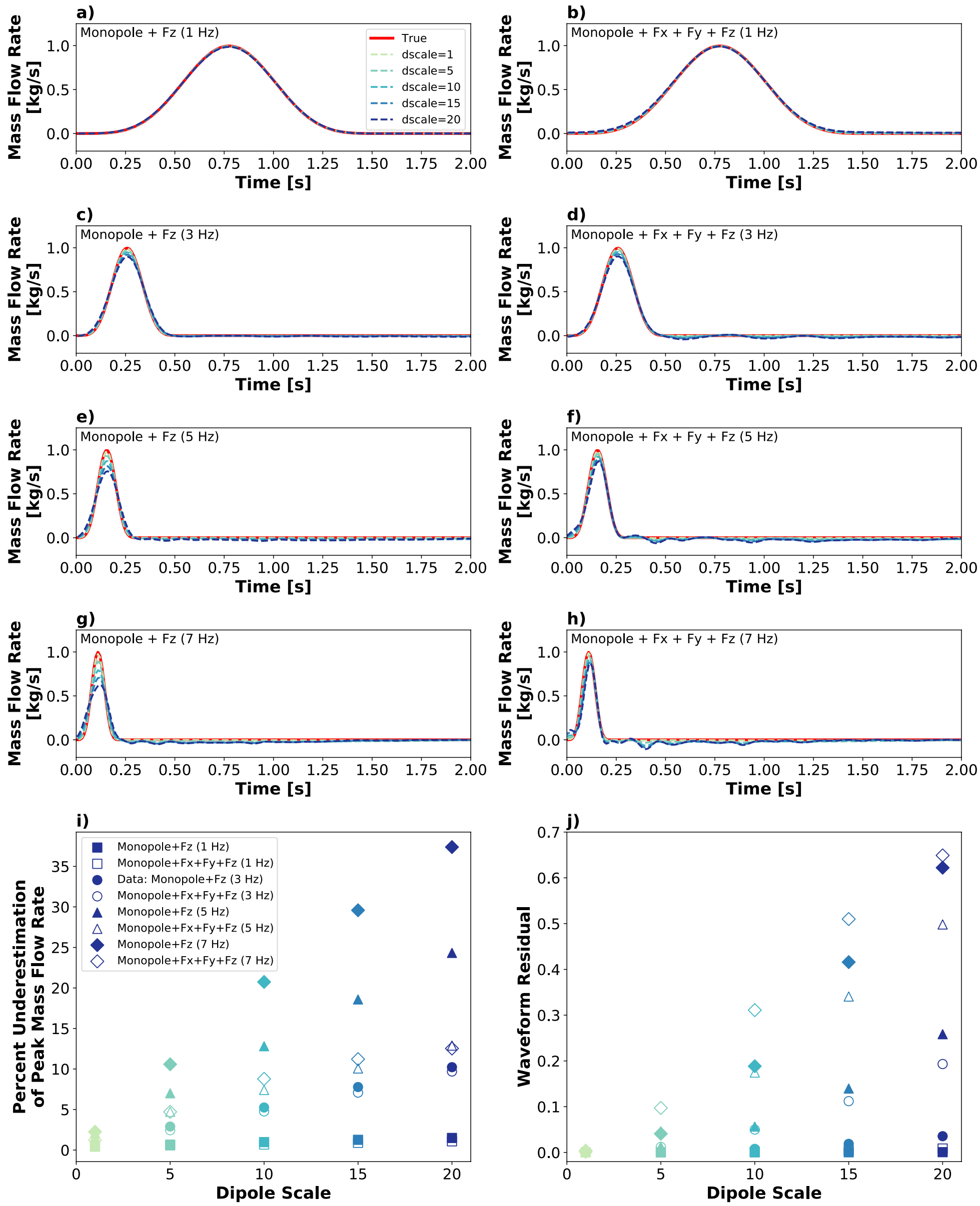

Figure 7. Inversion results for different source frequencies. Monopole-only source inversion for six stations placed on the crater rim spread equally in azimuth using (a, c, e and g) monopole + vertical dipole (monopole + F_z) and (b, d, f and h) monopole + slanted dipole (monopole + $F_x + F_y + F_z$) data for increasing dipole strengths relative to the monopole amplitude between 1 and 20. The source frequencies used are (a and b) 1 Hz, (c and d) 3 Hz, (e and f) 5 Hz, and (g and h) 7 Hz. The true solution is shown in red and the inversion solutions are shown using light to dark blue corresponding to increasing dipole scale relative to the monopole amplitude between 1 and 20. (i) Percent underestimation of the peak mass flow rate and (j) waveform residual for each inversion, where solid markers show results for inversions using monopole + vertical dipole (monopole + F_z) data and open face markers show results using monopole + slanted dipole (monopole + $F_x + F_y + F_z$) data.

varying source frequency. Therefore, the results presented in Figure 7 may indicate that the inversion solution is more accurate for data that are sampled at a higher resolution, not necessarily because of the change in frequency.

3.3.3. Monopole and Horizontal Dipole Inversions

Because infrasound deployments usually consist of infrasound sensors placed on the ground surface, the vertical dipole component is often neglected for waveform inversions due to insufficient sampling of the acoustic radiation in the vertical (e.g., De Angelis et al., 2016; Diaz-Moreno et al., 2019; Kim et al., 2012). We perform an

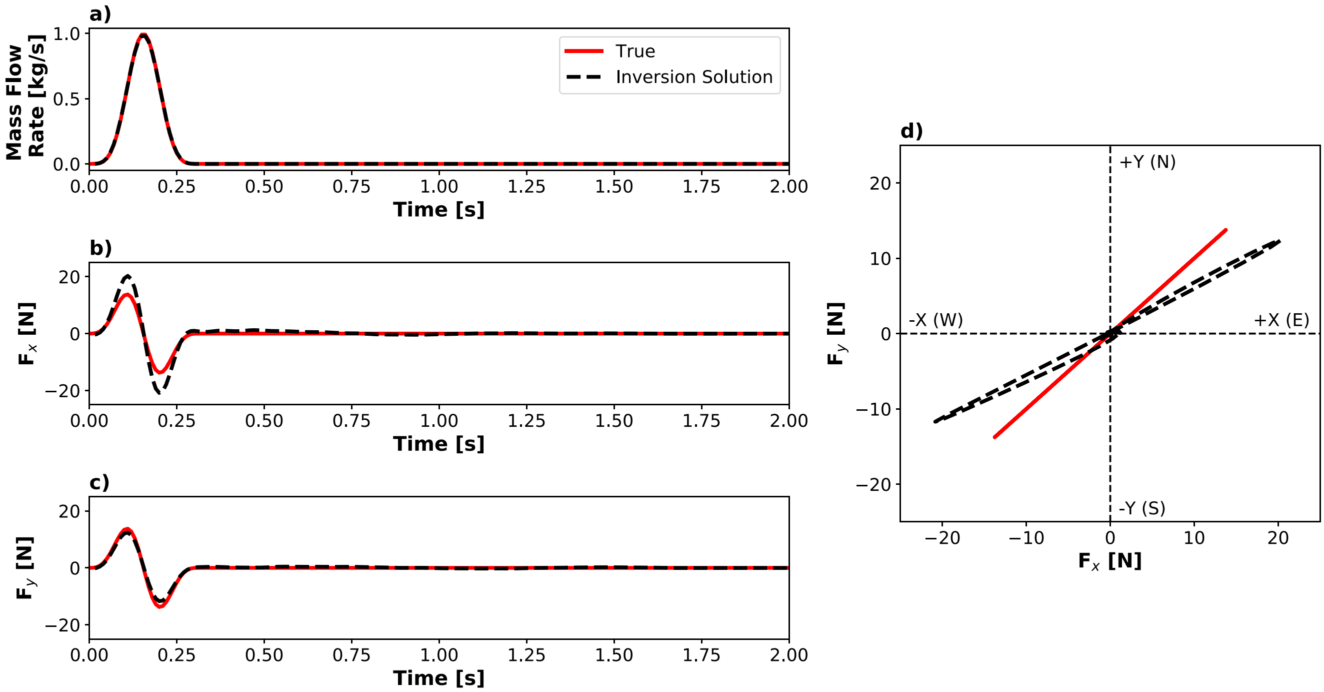

Figure 8. Inversion results for monopole and horizontal dipole components. Monopole + horizontal dipole inversion (monopole + $F_x + F_y$) for six stations placed on the crater rim spread equally in azimuth using monopole + slanted dipole data (monopole + $F_x + F_y + F_z$) without the addition of noise. The input source time functions are shown in red and inversion solutions in black for all panels. The source vectors are plotted for the (a) monopole (mass flow rate), and two horizontal dipole (force) components (b) x and (c) y. Panel (d) shows the horizontal dipole force components in map view.

inversion for the monopole and horizontal dipole component source vectors similar to the aforementioned studies but use data created from a multipole source (monopole and all three dipole components). Our results suggest that a dipole solution with the correct azimuth quadrant can be obtained, but the amplitude and exact direction of the dipole solution may not be correct if there is a substantial vertical dipole (F_z) component (Figure 8). For this particular example, the mass flow rate and F_y components are well recovered, however, the peak F_x is overestimated by 47.4%, yielding a dipole azimuth of 58.6° (13.6° deviation from true). The F_x component is less constrained than the F_y component due to the inclusion of a station directly in the +Y direction (SYN000) but not directly in the +X direction (SYN060 and SYN120 are 30° off the +X axis) in the inversion. In reality, it is difficult to imagine a dipole that is 100% horizontal in a volcanic setting (though an explosion in a tunnel or on the side of a cliff may be nearly horizontal), thus likely has at least some F_z component. We suggest that dipole results from studies such as Kim et al. (2012), De Angelis et al. (2016), and Diaz-Moreno et al. (2019) be interpreted with caution, as the infrasound multipole source inversion approach that neglects the vertical dipole component may not be a sufficient approach to determining the true acoustic dipole strength and azimuth.

3.3.4. Multipole Inversions With Increasing Number of Stations

Permanent and temporary infrasound deployments vary greatly in the number of infrasound stations deployed, as well as the configuration of that deployment. Multipole inversions are performed for an increasing number of stations (3–12) located on the crater rim spaced equally in azimuth surrounding the source, similar to a deployment where the purpose was to investigate potential source directionality. The solution vectors for these inversions are shown by Figures 9a–9d along with the waveform fits for the default deployment of 6 ground sensors (Figures 9e–9j). The mass flow rate solution vector (Figure 9a) can be well-resolved regardless of the number of stations around the source (3 or greater stations), even for a multipole inversion. These results agree with the stability of the mass flow rate solution for both monopole-only and multipole inversions, as shown by Iezzi et al. (2019). However, the dipole solution vectors (Figures 9b–9d) are not fully resolved, even in the absence of noise and for inversions with up to 12 stations placed around the source. For this example, the F_z component is underestimated by 20.5% from true for inversion using 12 stations. We note that the vertical dipole component (Figure 9d) is the most difficult to resolve using typical ground-based infrasound deployments, compared with

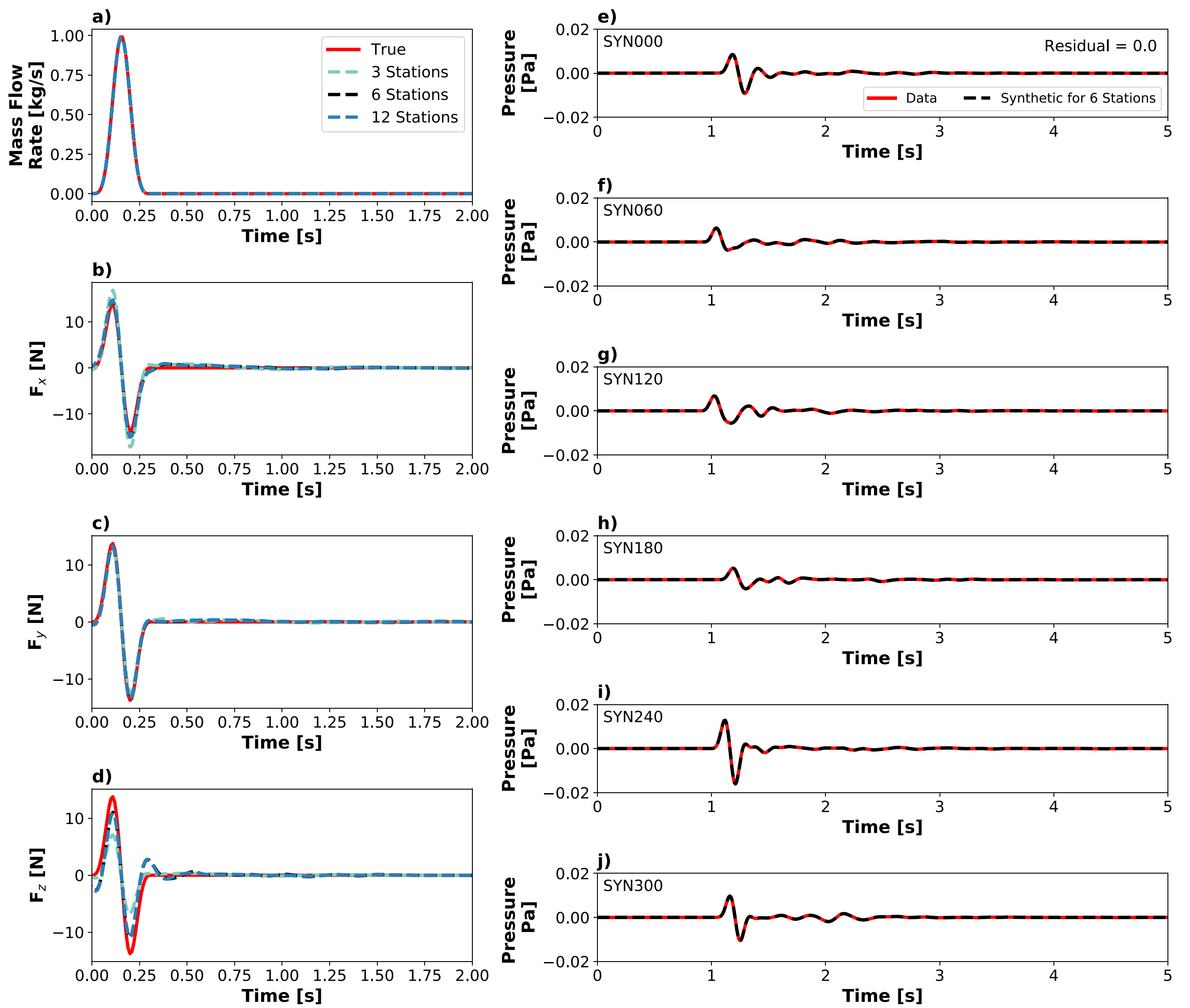

Figure 9. Inversion results for increasing number of stations. Monopole + slanted dipole source inversion (monopole + $F_x + F_y + F_z$) for an increasing number of stations using monopole + slanted dipole data (monopole + $F_x + F_y + F_z$) without the addition of noise. The number of synthetic stations include 3 (light blue), 6 (black), and 12 (dark blue) placed on the crater rim and spread equally in azimuth around the source. The input source time functions and data are shown in red for all panels. Source vectors are plotted for the (a) monopole (mass flow rate), and three dipole (force) components (b) x, (c) y, and (d) z. Panels (e–j) show the waveform fit for the inversion with 6 stations, yielding a residual of 0.0.

the horizontal dipole components (Figures 9b and 9c). Another outcome of this simple inversion test is that while the data can be fit perfectly with a residual of 0.0 (Figures 9e–9j, results for an inversion with 6 stations), an ill-posed inversion may not recover the correct solution vectors.

3.4. Realistic Inversions

Ideal inversion scenarios discussed so far are a necessary step to illuminate the limitations of multipole source inversions. However, observed data are likely more complex and may further complicate the inversion results. In this section, we introduce parameters of noise and wind to the data prior to inversions to mimic realistic scenarios and help understand their impact on the inversion results.

3.4.1. Noise

Noise is unavoidable for data collected in the field, so data analysis methods should be robust enough to handle at least some amount of noise in the data without compromising the results. We use data from a temporary deployment at Yasur volcano in 2016 (Iezzi et al., 2019; Jolly et al., 2017) during time periods when an explosion signal was not present in the data. The noise time series amplitudes are scaled relative to the maximum pressure of each synthetic data waveform by the specified SNR and added to the synthetic waveform in the time domain prior to inversion.

Increasing levels of noise are added to the synthetic data for both monopole-only (Figure 10a) and multipole inversions (Figures 10b–10e). The input data waveforms without noise and with a SNR of 5 are shown in Figures 10f–10k as an example. Inversions that include data with a SNR of 5 or greater produce reasonable source solutions for both the monopole-only and multipole inversions, with the exception of the vertical dipole component (Figure 10e). We note that this component was not resolved for inversions without noise (Figure 9d), so it is likely due to using a receiver configuration with 6 stations located on the crater rim. The source vector inversion solutions for all components approach the true source vectors for increasing SNR, as expected.

For comparison with the ideal inversion results in Section 3.3.1, we create synthetic data using a multipole source with an SNR of 10 but perform monopole-only inversions. We perform inversions that use the default real noise from a previous deployment at Yasur, as well as Gaussian noise (similar to Kim et al., 2012 who added 10% Gaussian random noise to the data prior to inversion for their testing). The addition of Gaussian noise yields results that are more similar to the noise free case (Figure 6c). The addition of real noise to the data for the specific scenario investigated results in a slightly lower percent underestimation of peak mass flow rate inversion solution (<2%, Figure 6c) but also follows a similar trend as the noise free case for increasing dipole strength. From this test we find that the type of noise added to the data prior to inversion may have an impact on the ability to resolve the mass flow rate solution, but results largely follow similar trends to the noise free case. Additionally, inversions in which real noise is added to the data also result in slightly higher residuals than the same inversion performed without noise or with Gaussian noise (Figure 6d).

3.4.2. Iterative Solver Settings

The waveform inversion procedure uses the LSQR iterative solver by Paige and Saunders (1982), as mentioned in Section 2.2. Because of this, settings that can affect the inversion solution include the number of iterations, which can be set to a specific value or determined by setting the residual tolerance over a certain number of iterations. We perform monopole-only (Figure 11a) and multipole (Figures 11b–11e) inversions where the number of iterations for LSQR is increased, similar to that of Iezzi et al. (2019). A SNR of 10 is added to the data prior to the inversions. Recall from Section 2.2 that the **G** matrix is an $m \times 4n$ matrix. For the network consisting of 6 stations, the size of our **G** matrix is $3{,}306 \times 500$ for monopole inversions and $3{,}306 \times 2{,}000$ for multipole inversions. The monopole-only inversion solution (Figure 11a) is very similar to the true solution regardless of the number of iterations performed (greater than five iterations), as observed by Iezzi et al. (2019). For iteration numbers between 5 and 100, the true source is resolved fairly well for all four source components (Figures 11b–11e). However, for iterations 500 and greater, "spurious forces" exist in all four components 0.5 s after the explosion onset due to overfitting of the data. We show the mean squared error (average squared difference between the inversion solution and true) for the inversion solution vectors with waveform residual for the mass flow rate (Figure 11f) and force (Figure 11g) vectors, where iteration numbers greater than 100 (denoted by a vertical lines in Figures 11f and 11g) result in increasing deviation from the true solution for all multipole inversion solution vectors. In general, we find that setting a residual tolerance of 0.01 over 10 iterations (usually resulting in less than 500 iterations) seems to be a good compromise between waveform fit and decreasing the introduction of spurious forces after the input force (after $T = 0.5$ s) that can be similar in amplitude to the true source.

3.4.3. Wind

In addition to noise, wind can also impact recorded infrasound signals even at local distances and therefore the ability to recover the acoustic source mechanism. However, wind is typically neglected in local acoustic waveform inversion studies (e.g., Diaz-Moreno et al., 2019; Fee et al., 2017; Iezzi et al., 2019; Kim et al., 2015). We perform a separate set of FDTD simulations in order to create synthetic data that includes wind of 10 m/s directed toward the East (+X), yielding a travel time decrease of ~0.025 s at ~300 m range for the station to the East (+X). The Green's functions remain the same as the previous inversions, where no wind is included. For this

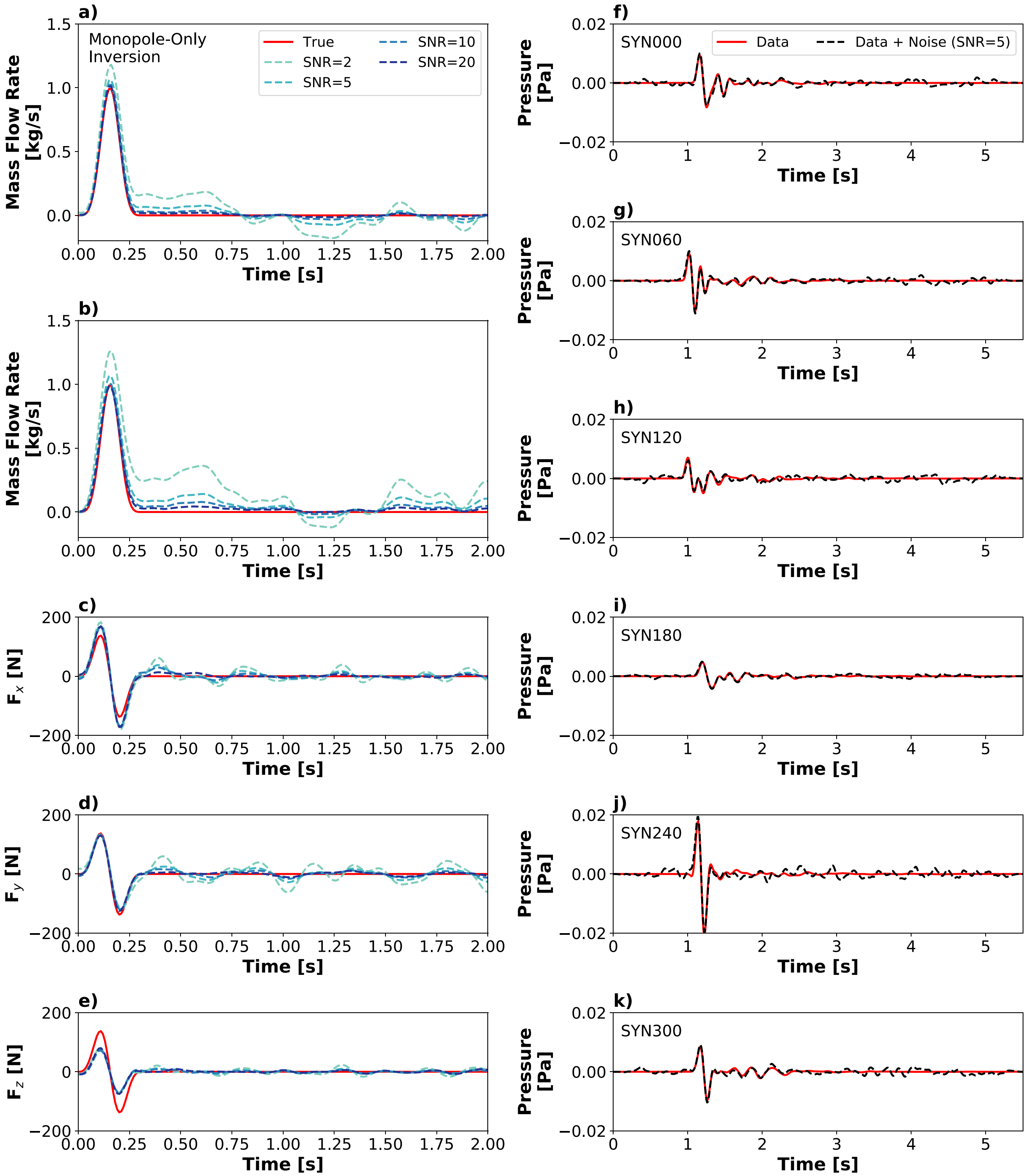

Figure 10. Monopole-only and multipole source inversion for increasing SNR. Monopole-only and monopole + slanted dipole source inversion results for 6 stations placed on the crater rim spread equally in azimuth using monopole-only and monopole + slanted dipole (monopole + F_x + F_y + F_z) data, respectively. The SNR levels include 2 (cyan), 5 (light blue), 10 (blue), and 20 (dark blue). The input source time functions are shown in red for all panels. Source vectors are plotted for the (a) monopole (mass flow rate) for the monopole-only inversion, (b) monopole (mass flow rate) for the multipole inversion, and three dipole (force) components (c) x, (d) y, and (e) z. Panels (f–k) show noise-free data (red) and data with a SNR of 5 added (black) waveforms.

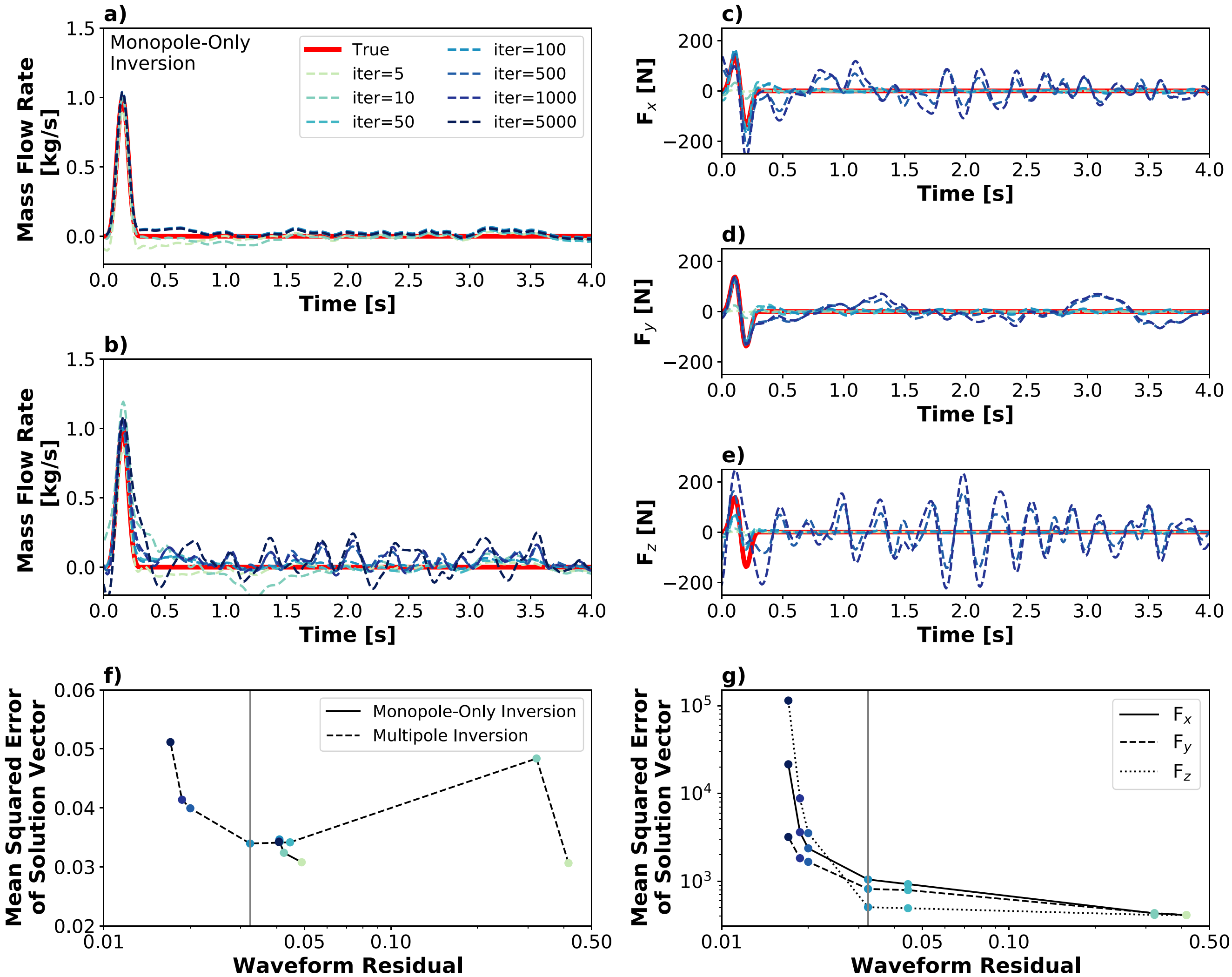

Figure 11. Inversion results for different iterative solver settings. Monopole-only and monopole + slanted dipole source inversion results for 6 stations placed on the crater rim spread equally in azimuth using monopole-only and monopole + slanted dipole (monopole + $F_x + F_y + F_z$) data, respectively, for increasing numbers of iterations. The number of iterations for LSQR range from 5 to 5000, shown from light to dark blue. The input source time functions are shown in red for all panels. Source vectors are plotted for the (a) monopole (mass flow rate) for the monopole-only inversion, (b) monopole (mass flow rate) for the multipole inversion, and three dipole (force) components (c) x, (d) y, and (e) z. Note: We do not plot the results for 5000 iterations in panels (c–e) due to their high amplitude. Mean squared error of the solution vectors for the (f) mass flow rate and (g) force vectors with waveform residual for inversion solutions for each number of iterations. The vertical lines in (f and g) denote the results at 100 iterations.

investigation, we only perform a monopole inversion as a simple investigation to focus on wind effects on the inversion. We refrain from performing multipole inversions or using a grid-search approach to limit the number of possible solutions to an already ill-posed multipole inversion.

The inversion procedure of Kim et al. (2015) allows for the user to specify the number of points that can be applied to shift the Green's functions in order to better fit the data. This allows the Green's functions and data to be time shifted by a certain amount during the inversion procedure to account for unresolved factors that can affect arrival time such as wind, sound speed, source/receiver location errors, etc. The first monopole inversion we perform sets this parameter to zero (i.e., no time shift is allowed in the inversion procedure). The explosion waveforms on stations to the East (e.g., SYN060 and SYN120, Figures 12c and 12d) arrive faster than expected by the windless Green's functions, while waveforms on the stations on the West (e.g., SYN240 and SYN300, Figures 12f and 12g) arrive slower than expected. This leads to a relatively high waveform residual (0.20) for this example since the main waveform energy does not line up and the peak mass flow rate is underestimated by 9.3% (Figure 12a). The second monopole inversion allows up to 10 points to be shifted between the Green's functions

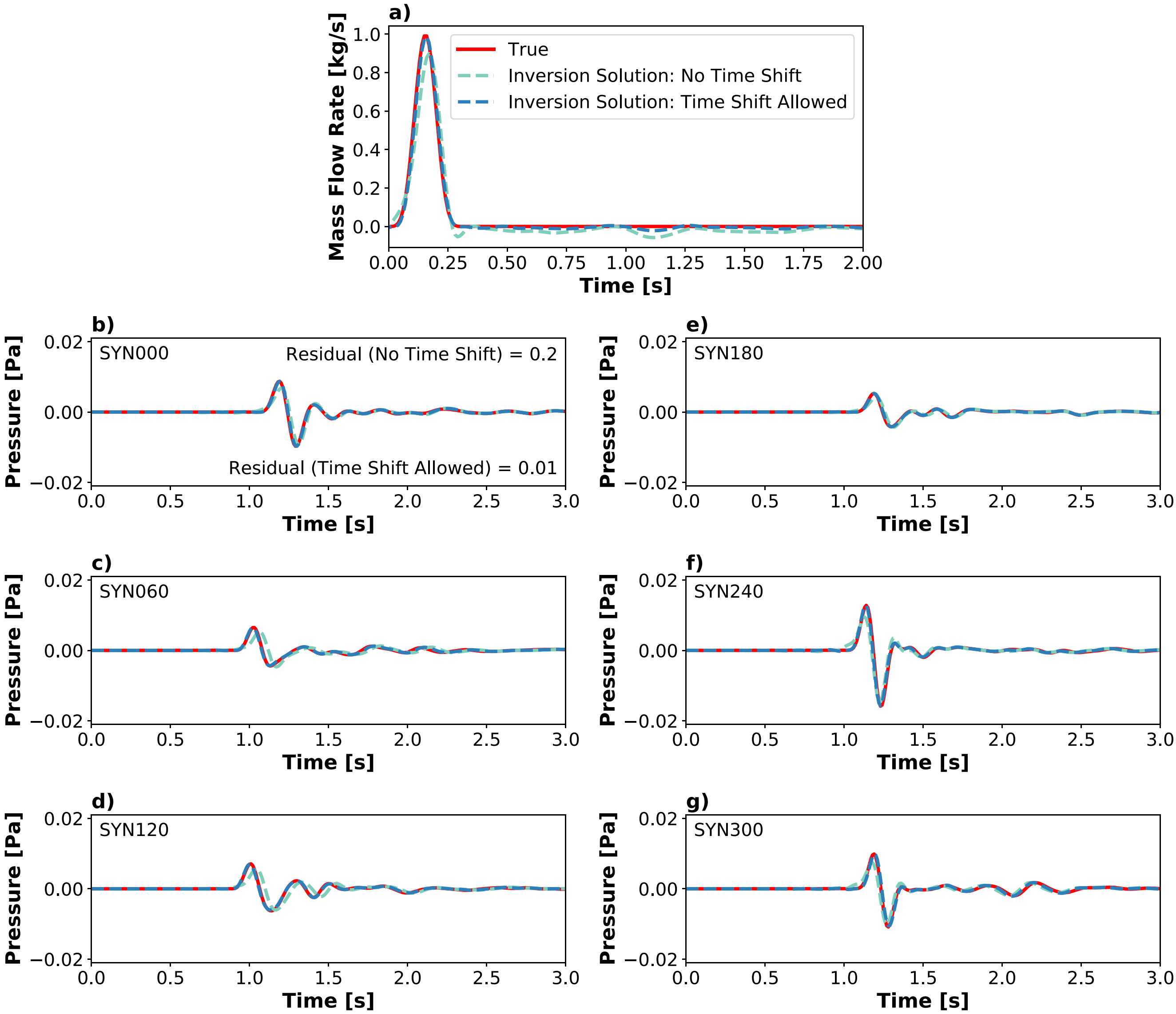

Figure 12. Inversion results that include wind. Monopole source inversion using monopole data that was created using an effective sound speed with 10 m/s wind directed toward the East for 6 stations placed on the crater rim spread equally in azimuth. Inversions are performed both without allowing for time shift in the data (light blue) and with allowing up to a 10**dt* = 0.1 s time shift (dark blue) for each station. The (a) monopole (mass flow rate) source vector, and (b–g) waveform fit is plotted for both inversions where the result without allowing for a time shift has a residual of 0.20 and the inversion that allows for a time shift has a residual of 0.01.

and data (time shift of 10**dt* = 0.1 s). The time shift allows for the waveforms to line up properly, lowers the waveform residual to 0.01 (Figures 12b–12g), and allows the inversion to recover the mass flow rate solution well (Figure 12a). From this simple test, we find that the use of an appropriate value of allowable time shift may minimize the impacts of wind on the potential infrasound travel time discrepancies and therefore improve the ability to resolve the proper source vector for monopole-only inversions.

3.5. Multipole Solution: Azimuth, Inclination, and Rectilinearity

Previous studies such as Kim et al. (2012), Iezzi et al. (2019), and Diaz-Moreno et al. (2019) aimed to investigate the stability and significance of the dipole component for multipole inversions. Kim et al. (2012) used consistent dipole solution azimuth as one metric to investigate the dipole solution, though they note that the dipole they find might be due to topography since they did not incorporate 3-D Green's functions for their propagation term. Iezzi et al. (2019) found that rectilinearity of the dipole solution may be an effective way to help quantify the whether the inversion dipole solution is real or just fitting noise. The rectilinearity is defined as (Montalbetti & Kanasewich, 1970)

$$F_r = 1 - \frac{\lambda_2}{\lambda_1} \quad (4)$$

where λ_1 is the principal eigenvalue (i.e., a measure of the long axis) and λ_2 is the second eigenvalue (i.e., a measure of the short axis). This equation yields results between 0 and 1, where $F_r = 1$ represents purely rectilinear motion. If a dipole is a directed force, then it should have high rectilinearity. However, we caution that just because rectilinearity is high doesn't mean the dipole should be considered real (e.g., results from Kim et al., 2012).

We show the results for a multipole inversion that uses 6 stations on the crater rim, a SNR of 10 added to the data, and a dipole scale of 10 relative to the peak mass flow rate of 1 kg/s in Figure 13. The calculations of rectilinearity, azimuth, and inclination in Figure 13 are performed at each data point and including the previous 7 and subsequent 7 data points as a means of slightly smoothing the calculation results and making them easier to interpret. The horizontal dipole solution vector results show pretty good agreement with the input solution (Figures 13a and 13b), with less agreement for the vertical dipole component (Figure 13c). The dipole strength, defined as the square root of the sum of the squares of the three individual components, is shown by Figure 13d. During the period of high dipole strength (T = 0–0.3 s, gray shaded region of Figure 13d), the rectilinearity remains close to 1 and relatively stable (Figure 13e). Iezzi et al. (2019) chose to use a stable rectilinearity value over a 1 s time period, which corresponded to the highest-amplitude oscillations of the dipole component in their study. This is similar to the period of high dipole strength in this example (T = 0.0–0.3 s, gray shaded region of Figure 13d). During this period the dipole azimuth is stable but reverses 180° halfway through (Figure 13f), while the dipole inclination remains stable throughout (Figure 13g). The rectilinearity value is close to 1 in other time periods, but is not stable or correlated with the other calculations. The dipole azimuth pattern is similar in other time periods, but is not accompanied by high dipole strength, or stable rectilinearity and inclination. Although the dipole inclination is stable during T = 0–0.3 s, it is lower than expected (~20° compared to 35°) due to lower amplitude vertical dipole component from only using sensors placed on the surface for the inversions. We therefore suggest that a stable rectilinearity close to 1 over some time period, coupled with high dipole strength, an azimuth that indicates the amplitude oscillates between positive and negative, and stable inclination may indicate a true dipole inversion solution.

4. Discussion

This study provides insight into multipole infrasound waveform inversion solutions through simulated examples, investigated primarily with a 5 Hz source. In general, infrasound full waveform inversion is robust in quantifying simple explosion sources (monopole), including those of anthropogenic and volcanic origin, using network deployments of infrasound sensors placed around a source. However, care should be taken when analyzing and interpreting results from more complex acoustic sources (multipole) that have significant directional components. The parameters used for each inversion scenario are summarized in Table 1 along with the main result for each investigation. Prior to relying on multipole inversion results, we show that it is clearly beneficial to complete a synthetic study such as that presented here as part of field deployment planning to determine how well a simple solution vector can be recovered with a given station configuration and estimated source type.

4.1. Simple Inversions

Network geometry and station location relative to the dipole source orientation can impact the ability to recover the mass flow rate and dipole force solutions. In the absence of topography, sensors placed on a flat plane will not record radiation from a vertical dipole source also located on the plane (Figure 3). However, in the case of pronounced topography such as that from a volcanic crater, sensors placed on the ground surface can record some amount of radiation from the vertical dipole. This makes it difficult to separate the effects from the vertical dipole from the horizontal dipole for certain network geometries. While increasing the number of stations at various azimuths can help constrain the potential directional source, this is not always a feasible scenario for the monitoring of explosive sources such as volcanoes. For scenarios in which monopole-only inversions are performed but data are created from a multipole source using a single station, we find that the recovered mass flow rate solution

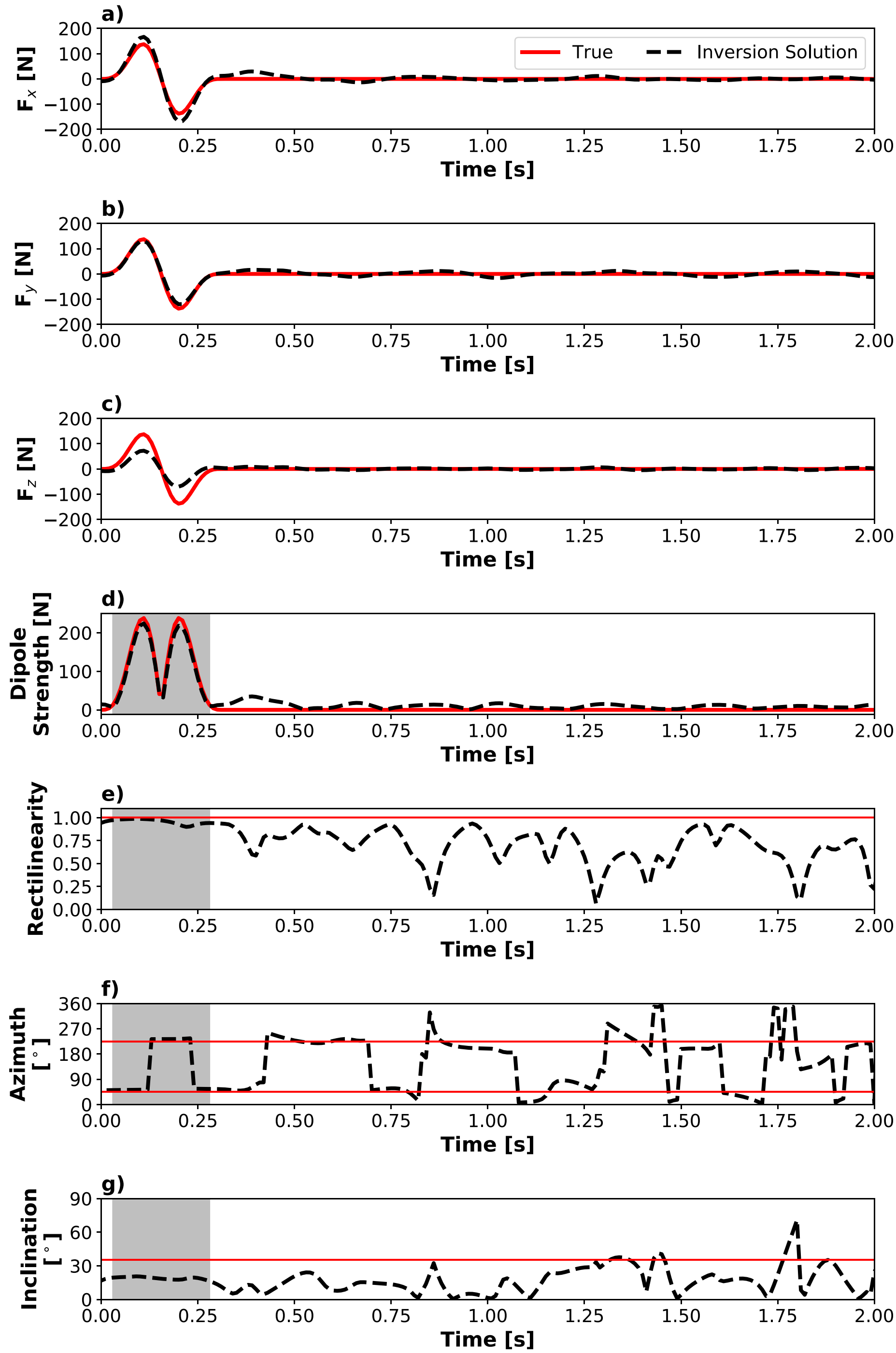

Figure 13. Inversion results to investigate azimuth, inclination, and rectilinearity of the dipole solution. Monopole + slanted dipole source inversion (monopole + $F_x + F_y + F_z$) for 6 stations placed on the crater rim spread equally in azimuth using monopole + slanted dipole (monopole + $F_x + F_y + F_z$) data with dipole scale of 10 and noise added with a SNR of 10. The input source time functions are shown as red solid lines and inversion solution as black dotted lines for all panels. Source vectors for the dipole (force) components (a) x, (b) y, (c) z, and (d) dipole strength, as well as calculated (e) rectilinearity, (f) dipole azimuth, and (g) dipole inclination. Calculations are performed at each data points using the previous 7 and subsequent 7 data points. The shaded region in (d–g) shows the area where the dipole solution is real (T = 0–0.3 s). The red horizontal lines in (e), (f), and (g) indicate perfectly rectilinear motion, true dipole azimuths (45° and 225°), and true dipole inclination (35.25°), respectively.

is dependent on the azimuth at which the station is placed relative to the dipole azimuth (Figure 4). When the default deployment of 6 stations are equally spaced around the source and there is no topography (Figures 5a–5d), the mass flow rate solution for both the monopole + vertical dipole data (Figure 5a) and monopole and all three dipole components (monopole + slanted dipole) are nearly the true solution. In this scenario, the overestimations of amplitude to the northeast "cancel out" the underestimations of amplitude to the southwest, causing the solution to be an average and thus close to the true solution. However, if a deployment is not symmetrical and the sensors are grouped on the East side of the source only (Figures 5e–5h), the mass flow rate solution for monopole inversions that use monopole + slanted dipole data begin to show differences (Figure 5g). Therefore, the network geometry may have an impact on the recovered source time functions from directional sources, even for monopole inversions.

4.2. Application of Inversions to the Topography of Yasur Volcano, Vanuatu

Monopole-only inversions are the most common infrasound inversions performed in recent studies and can provide essential information including explosion yield and mass flow rate (e.g., Fee et al., 2017; Johnson et al., 2008; Johnson & Miller, 2014; Kim et al., 2015). Monopole inversions that incorporate 3-D numerical Green's functions using realistic topography generally provide a good fit to the data with residuals of ~0.05 (Kim et al., 2015) and <0.15 (Fee et al., 2017) for Vulcanian explosions at Sakurajima volcano, Japan. Additionally, erupted mass estimates in these inversions agree reasonably well with independent calculations using measurements of ash and gas emissions (Fee et al., 2017). Kim and Rodgers (2016) apply a similar monopole inversion method incorporating realistic atmospheric conditions and topography to chemical explosions and find explosion yield estimates in good agreement with actual yields with residuals <0.04. In the present study, monopole inversions are reliable with SNR greater than 5 (Figure 10a), at least three stations spread out in azimuth (Figure 9a) (also shown in Kim et al., 2012), and are not strongly dependent on the number of iterations of the LSQR solver (Figure 11a). While monopole-only inversions for monopole sources appear to be a good way to retrieve the mass flow rate, there are likely cases in which a dipole component may be present but a monopole inversion may be sufficient. For example, for monopole inversions that use data from a multipole source, the solution may be sufficient when the dipole component is small (Figure 6). We also note that the ability to resolve the mass flow rate solution increased when the number of samples per period increased (i.e., for decreasing source frequency with constant *dt*, Figure 7), meaning that sampling frequency may impact the recovered solution and should be considered for future deployments.

Multipole inversions allow for a more in depth understanding of potentially directional acoustic sources such as those from complex volcanic explosions (e.g., Iezzi et al., 2019; Johnson et al., 2008; Jolly et al., 2016, 2017), buried chemical explosions (e.g., Blom et al., 2020; Kim et al., 2020), and mass movements (e.g., Johnson et al., 2021). Recent studies (e.g., Blom et al., 2020; Kim et al., 2020) have found that acoustic wavefields created by underground explosions have strong vertical directionality which cannot be accounted for by a simple monopole source. This can affect the ability to estimate explosion yield and depth of burial if this directionality is not accounted for. For volcanoes, acoustic directionality has been shown to agree well with ballistic trajectories from explosions from Yasur volcano, Vanuatu (Iezzi et al., 2019; Jolly et al., 2017) and with bubble burst eruptions in the crater lake of White Island, New Zealand (Jolly et al., 2016). However, due to infrasound deployments typically being constrained to Earth's surface, studies have focused on inversions that include the monopole and horizontal dipole (no vertical dipole, Kim et al., 2012; Diaz-Moreno et al., 2019) or have included the vertical dipole in inversions but found them to be ill-posed, even with an infrasound sensors aboard a tethered aerostat (Iezzi et al., 2019). While the idea of only solving for the monopole and horizontal component of the dipole is appealing, we show that both the amplitude and azimuth of the dipole solution may not be correct if the data are produced by a source with a significant vertical dipole component (Figure 8). Therefore, network geometries where the vertical wavefield is not sufficiently sampled may limit the value of the multipole inversion approach. We find that in some cases the mass flow rate solution vector can be resolved more accurately than the dipole components for ill-posed multipole inversions (e.g., Figures 8a, 9a, and 11b), consistent with the findings of Iezzi et al. (2019). Increasing the number of stations placed on the crater rim can allow for the mass flow rate and horizontal dipole forces to be more fully resolved (Figures 9a–9c), but even with 12 stations the vertical dipole cannot be resolved (Figure 9d). We reiterate that a waveform misfit (residual) of 0.0 does not mean that the unique and correct solution is recovered for ill-posed inversions such as for the multipole infrasound source (Figure 9).

10.1029/2021JB023223

The presence of noise further complicates the recovered solution for multipole inversions. Inversions performed that incorporate an increasing SNR show that an SNR of five or greater allows for the simple sources used here to be resolved, with the exception of the vertical dipole force (Figure 10). Similar to the findings of Iezzi et al. (2019), we find that multipole inversions with insufficient wavefield sampling can lead to "spurious forces" if the number of iterations for LSQR is too high (Figures 11c–11e). In other words, pushing the inversion solution to fit the data too well can result in unstable, or meaningless solutions. This is in good agreement with the original LSQR solver paper by Paige and Saunders (1982), where it was noted that convergence to an acceptable solution can occur but the solution may begin to change and grow rapidly if iterations are allowed to continue. A similar phenomena of the introduction of spurious forces was seen in the seismic inversions of Bean et al. (2008).

Similar to general noise in data, environments such as volcanoes can be prone to wind, especially those with high summit altitudes. Wind can impact infrasound propagation even at local distances (e.g., Kim & Rodgers, 2017), which in turn can affect the ability to perform infrasound source inversions. In this study, we find that during modest wind conditions of 10 m/s, monopole inversions that do not allow for a time shift between the data and Green's functions result in a waveform residual of 0.20. However, allowing for a small time shift in the inversion procedure that encompasses the impact of the wind speed on arrival time allows for the waveform residual to be reduced to 0.01 and solution vector to be resolved. Therefore, the use of an appropriate value of allowable time shift may minimize the impacts of wind on the potential infrasound travel time discrepancies and improve the ability to resolve the proper source vector for monopole-only inversions. In our example, the source location was fixed so an appropriate time shift value needed to be as large as the potential timing errors between the Green's functions and data (e.g., larger than the impact of wind on the travel time). However, including an allowable time shift may adversely affect the inversion in some situations, such as if the source location is unknown. We refrain from performing multipole inversions or using a grid-search approach because the allowable time shift value introduces more possible solutions to an already ill-posed multipole inversion (e.g., Iezzi et al., 2019).

We find that rectilinearity alone may not be sufficient to quantify the existence of a real dipole, but that a combination of a stable rectilinearity close to 1 over some time period, coupled with high dipole strength, an azimuth that indicates amplitude oscillations between positive and negative, and stable inclination may indicate a true dipole (Figure 13). Another popular method to determine the inversion with optimal number of model parameters is the Akaike Information Criterion (AIC) (Ohminato et al., 1998). However, Iezzi et al. (2019) found that of the 80 events at Yasur volcano used for multipole waveform inversions, 65 yielded smaller AIC values for inversions using all four components even though the inversions were ill-posed, showing that AIC does not always yield the "best" solution and should be used with caution (Bean et al., 2008; Iezzi et al., 2019). Additionally, Kim et al. (2012) use the condition number (ratio of largest and smallest eigenvalues of G^TG) to help quantify the stability of multipole (monopole + horizontal dipole) inversion results, where a high condition number can indicate less stable solutions.

4.3. Limitations of the Study

Synthetic inversion studies can increase understanding of the limitations of multipole infrasound inversions based on specific deployment scenarios. Our study allows for a deeper understanding of infrasound multipole inversions, including situations in which the source can confidently be recovered, as well as scenarios in which the source vectors may be less reliable. Due to the simplicity of the synthetic scenarios, there are some limitations to this study. The inversion method used here assumes linear wave propagation as opposed to nonlinear (e.g., Maher et al., 2020), which is adequate for the low amplitudes used here and appears to be valid for other recent studies (Fee et al., 2017; Iezzi et al., 2019; Kim et al., 2015). In our study, we assumed that the DEM used for FDTD modeling was sufficiently accurate and that the source location was known, both of which may not be true. For realistic scenarios, the DEM may not accurately capture the true topography, especially at frequently active volcanoes where residual ash and gas may exist within the crater obscuring direct views, which may hinder the ability to create high-resolution DEMs (~1–2 m) using visible band imagery. High-resolution DEMs of the volcanic crater may also be merged with lower resolution DEMs to increase the spatial coverage (e.g., Iezzi et al., 2019) which can also introduce errors including seams from merging the DEM datasets. Additionally, for some volcanoes the crater morphology and topography can change over short time scales due to frequent explosions and/or mass wasting events which may not be captured by the DEM. In addition to the accuracy of the DEM impacting the resultant numerical Green's functions, the FDTD method used here assumes a rigid boundary which may not always be a good assumption (e.g. Bishop et al., 2021; Matoza et al., 2009). Numerical models that represent a smoothly varying topographic surface using stairstep boundaries may introduce spurious scattering into the modeled Green's functions (e.g., de Groot-Hedlin, 2004). We incorporate the multipole source (monopole and dipole) to allow for more complex source mechanisms, but note that the results are only valid for short duration explosive sources. Higher order source terms such as the quadrupole are beyond the scope of this study and we refer to Matoza et al. (2013) for more discussion on the quadrupole source. We note that linking equivalent source representations derived from waveform inversion to complex arbitrary sources (e.g., Brogi et al., 2018; Lacanna & Ripepe, 2020; Matoza et al., 2013) is a goal of future research. Additionally, we use a point-source assumption which is likely invalid at close range for large spatially extended sources (e.g., Matoza et al., 2013). Future work could investigate longer duration volcanic eruptions and other topographic environments (e.g., larger stratovolcanoes), as many of the results presented in this study are specific to the explosion type and topography of Yasur volcano.

Because this was a synthetic study we were able to place sensors wherever we desired, which may not be possible for field deployments due to limitations of accessibility and safety. Due to the focus of this study on resolving the multipole source, network geometries examined used single sensors placed around the explosion source to maximize azimuthal coverage. We touch upon non-symmetrical network deployments in Section 3.2.2 and find that uneven network spacing can bias the inversion solutions. Additionally, we investigated the impact of SNR on the ability to recover the source time functions, which eludes to the impact of performing inversions with stations that are further from the source and therefore have lower SNR. Future work could continue investigating other network geometry types and sensor groupings (e.g., arrays) that may be placed in more realistic and accessible locations based on the intended study location.

5. Conclusions

We perform both monopole and multipole (monopole and dipole) synthetic infrasound source inversions using 3-D Green's functions to investigate the ability to adequately resolve the source time functions and their relative amplitudes for a variety of infrasound deployment scenarios. We find that a monopole inversion with a ground-based network yields information that may be good enough for practical purposes (<10% underestimation of the peak mass flow rate), even for multipole sources as long as the dipole component is relatively small (dipole strength <5 times relative to the monopole) and the network geometry is sufficient. If multipole inversions are to be performed using only sensors placed on the ground surface, care should be taken in interpreting the results, even if only the horizontal dipole source components are used in the inversion. A combination of a stable rectilinearity close to 1 over some time period, high dipole strength, an azimuth that indicates amplitude oscillations between positive and negative, and stable inclination may indicate a true dipole inversion solution. We stress that because multipole inversions are ill-posed for many deployments, a low residual does not necessarily mean that the proper source vector has been recovered. As articulated by Bean et al. (2008), observations cannot be used to verify models but only to falsify them (no amount of observational fits prove the model, one misfit falsifies it). We suggest that studies such as this using a variety of sensor configurations can help investigate the limitations and place bounds on how much information may be missing, including the likely source mass flow rate inversion solution underestimation.

We chose to use an idealized volcanic explosion acoustic source function represented by a Blackman-Harris window function in this study, as volcanic topography and likely source time functions are expected to be more complex than their anthropogenic counterparts. We note that for this type of study, the input source characteristics and topographic environment are less important than our ability to recover the input source time functions for a given scenario. Finally, our work provides a useful way to develop and assess networks and optimize the value of the data they collect. While portions of this study have specific value for future deployments at Yasur, the techniques and tools developed here can be utilized to improve the data collection worldwide. Such techniques will improve assessments of eruption size and directionality from real-time infrasound monitoring data of volcanoes, as well as improve estimates of explosion yield and depth of burial for anthropogenic explosions.

Data Availability Statement

The infraFDTD3D source code is available upon request to K.K. A DEM of the Yasur crater can be accessed on OpenTopography (https://doi.org/10.5069/G90V89XD, R. Fitzgerald, 2019).

Acknowledgments
The authors acknowledge support from NSF Grants EAR-1952392 (A.M.I.) and EAR-1847736 (R.S.M.). D.F. acknowledges support from the Alaska Volcano Observatory through the U.S. Geological Survey Volcano Hazards Program. The authors would like to thank Jeffrey Johnson, Kate Allstadt, and an anonymous reviewer for helpful reviews of this manuscript as well as Editor Yehuda Ben-Zion.

References

Bean, C., Lokmer, I., & O'Brien, G. (2008). Influence of near-surface volcanic structure on long-period seismic signals and on moment tensor inversions: Simulated examples from Mount Etna. *Journal of Geophysical Research*, *113*(B8). https://doi.org/10.1029/2007JB005468

Bishop, J. W., Fee, D., Modrak, R., Tape, C., & Kim, K. (2021). Spectral Element Modeling of Acoustic to Seismic Coupling over Topography. *Journal of Geophysical Research: Solid Earth*. https://doi.org/10.1029/2021jb023142

Blom, P., Iezzi, A. M., & Euler, G. (2020). Seismoacoustic analysis of underground explosions using the Rayleigh integral. *Geophysical Journal International*, *223*(2), 1069–1085. https://doi.org/10.1093/gji/ggaa363

Bowman, D. C., & Lees, J. M. (2015). Infrasound in the middle stratosphere measured with a free-flying acoustic array. *Geophysical Research Letters*, *42*(10). https://doi.org/10.1002/2015GL066570

Brissaud, Q., Martin, R., Garcia, R. F., & Komatitsch, D. (2017). Hybrid Galerkin numerical modelling of elastodynamics and compressible Navier-Stokes couplings: Applications to seismo-gravito acoustic waves. *Geophysical Journal International*, *210*(2), 1047–1069. https://doi.org/10.1093/gji/ggx185

Brogi, F., Ripepe, M., & Bonadonna, C. (2018). Lattice Boltzmann modeling to explain volcano acoustic source. *Scientific Reports*, *8*, 1–8. https://doi.org/10.1038/s41598-018-27387-0

De Angelis, S., Diaz-Moreno, A., & Zuccarello, L. (2019). Recent developments and applications of acoustic infrasound to monitor volcanic emissions. *Remote Sensing*, *11*(11), 1–18. https://doi.org/10.3390/rs11111302

De Angelis, S., Lamb, O. D., Lamur, A., Hornby, A. J., von Aulock, F. W., Chigna, G., et al. (2016). Characterization of moderate ash-and-gas explosions at Santiaguito volcano, Guatemala, from infrasound waveform inversion and thermal infrared measurements. *Geophysical Research Letters*, *43*(12), 6220–6227. https://doi.org/10.1002/2016GL069098

de Groot-Hedlin, C. D. (2004). Criteria for discretization of seafloor bathymetry when using a stairstep approximation: Application to computation of T-phase seismograms. *Journal of the Acoustical Society of America*, *115*(3), 1103–1113. https://doi.org/10.1121/1.1643361

de Groot-Hedlin, C. D. (2016). Long-range propagation of nonlinear infrasound waves through an absorbing atmosphere. *Journal of the Acoustical Society of America*, *139*(4), 1565–1577. https://doi.org/10.1121/1.4944759

Diaz-Moreno, A., Iezzi, A. M., Lamb, O. D., Fee, D., Kim, K., Zuccarello, L., & De Angelis, S. (2019). Volume flow rate estimation for small explosions at Mt. Etna, Italy, from acoustic waveform inversion. *Geophysical Research Letters*, *46*(20), 11071–11079. https://doi.org/10.1029/2019GL084598

Fee, D., Izbekov, P., Kim, K., Yokoo, A., Lopez, T., Prata, F., et al. (2017). Eruption mass estimation using infrasound waveform inversion and ash and gas measurements: Evaluation at Sakurajima Volcano, Japan. *Earth and Planetary Science Letters*, *480*, 42–52. https://doi.org/10.1016/j.epsl.2017.09.043

Fee, D., & Matoza, R. S. (2013). An overview of volcano infrasound: From Hawaiian to Plinian, local to global. *Journal of Volcanology and Geothermal Research*, *249*, 123–139. https://doi.org/10.1016/j.jvolgeores.2012.09.002

Fee, D., Toney, L., Kim, K., Sanderson, R. W., Iezzi, A. M., Matoza, R. S., et al. (2021). Local explosion detection and infrasound localization by reverse time Migration using 3-D finite-difference wave propagation. *Frontiers in Earth Science*, *9*. https://doi.org/10.3389/feart.2021.620813

Fitzgerald, R. H. (2019). Yasur Volcano Crater DEM, Republic of Vanuatu. In *Distributed by opentopography*. https://doi.org/10.5069/G90V89XD

Fitzgerald, R. H., Kennedy, B. M., Gomez, C., Wilson, T. M., Simons, B., Leonard, G. S., et al. (2020). Volcanic ballistic projectile deposition from a continuously erupting volcano: Yasur Volcano, Vanuatu. *Volcanica*, *3*(2), 183–204. https://doi.org/10.30909/vol.03.02.183204

Iezzi, A. M., Fee, D., Haney, M. M., & Lyons, J. J. (2020). Seismo-Acoustic Characterization of Mount Cleveland Volcano Explosions. *Frontiers in Earth Science*, *8*, 1–19. https://doi.org/10.3389/feart.2020.573368

Iezzi, A. M., Fee, D., Kim, K., Jolly, A. D., & Matoza, R. S. (2019). Three-Dimensional acoustic multipole waveform inversion at Yasur Volcano, Vanuatu. *Journal of Geophysical Research: Solid Earth*, *124*(8), 8679–8703. https://doi.org/10.1029/2018jb017073

Ishii, K., Yokoo, A., Iguchi, M., & Fujita, E. (2020). Utilizing the solution of sound diffraction by a thin screen to evaluate infrasound waves attenuated around volcano topography. *Journal of Volcanology and Geothermal Research*, *402*, 106983. https://doi.org/10.1016/j.jvolgeores.2020.106983

Jensen, F. B., Kuperman, W. A., Porter, M. B., & Schmidt, H. (2011). *Computational ocean acoustics* (2nd ed.). Springer. Retrieved From https://doi.org/10.1007/978-1-4419-8678-8

Johnson, J. B. (2019). Local volcano infrasound monitoring. In A. Le Pichon, E. Blanc, & A. Hauchecorne (Eds.), *Infrasound monitoring for atmospheric studies* (pp. 989–1022). Springer. https://doi.org/10.1007/978-3-319-75140-5_32

Johnson, J. B., Anderson, J. F., Marcillo, O., & Arrowsmith, S. (2012). Probing local wind and temperature structure using infrasound from Volcan Villarrica (Chile). *Journal of Geophysical Research*, *117*(17), 1–16. https://doi.org/10.1029/2012JD017694

Johnson, J. B., Anderson, J. F., Marshall, H. P., Havens, S., & Watson, L. M. (2021). Snow Avalanche Detection and Source Constraints Made Using a Networked Array of Infrasound Sensors. *Journal of Geophysical Research: Earth Surface*, *126*(3), 1–24. https://doi.org/10.1029/2020JF005741

Johnson, J. B., Aster, R., Jones, K. R., Kyle, P., & McIntosh, B. (2008). Acoustic source characterization of impulsive Strombolian eruptions from the Mount Erebus lava lake. *Journal of Volcanology and Geothermal Research*, *177*(3), 673–686. https://doi.org/10.1016/j.jvolgeores.2008.06.028

Johnson, J. B., & Miller, A. J. C. (2014). Application of the monopole source to quantify explosive flux during vulcanian explosions at Sakurajima Volcano (Japan). *Seismological Research Letters*, *85*(6), 1163–1176. https://doi.org/10.1785/0220140058

Jolly, A. D., Kennedy, B., Edwards, M., Jousset, P., & Scheu, B. (2016). Infrasound tremor from bubble burst eruptions in the viscous shallow crater lake of White Island, New Zealand, and its implications for interpreting volcanic source processes. *Journal of Volcanology and Geothermal Research*, *327*, 585–603. https://doi.org/10.1016/j.jvolgeores.2016.08.010

Jolly, A. D., Matoza, R. S., Fee, D., Kennedy, B., Iezzi, A. M., Fitzgerald, R. H., et al. (2017). Capturing the acoustic radiation pattern of strombolian eruptions using infrasound sensors aboard a tethered aerostat, Yasur volcano, Vanuatu. *Geophysical Research Letters*, *44*(19), 9672–9680. https://doi.org/10.1002/2017GL074971

Kennett, B., & Fichtner, A. (2020). *Exploiting seismic waveforms: Correlation, heterogeneity and inversion*. Cambridge University Press.

Kim, K., Bowman, D. C., & Fee, D. (2020). Acoustic wave generation by finite surface motions simulated by full 3-D finite difference method. *American Geophysical Union Fall Meeting*.

Kim, K., Fee, D., Yokoo, A., & Lees, J. M. (2015). Acoustic source inversion to estimate volume flux from volcanic explosions. *Geophysical Research Letters*, *42*(13), 5243–5249. https://doi.org/10.1002/2015GL064466

Kim, K., & Lees, J. M. (2011). Finite-difference time-domain modeling of transient infrasonic wavefields excited by volcanic explosions. *Geophysical Research Letters*, *38*(6). https://doi.org/10.1029/2010GL046615

Kim, K., & Lees, J. M. (2014). Local volcano infrasound and source localization investigated by 3D simulation. *Seismological Research Letters*, *85*(6), 1177–1186. https://doi.org/10.1785/0220140029

Kim, K., Lees, J. M., & Ruiz, M. (2012). Acoustic multipole source model for volcanic explosions and inversion for source parameters. *Geophysical Journal International*, *191*(3), 1192–1204. https://doi.org/10.1111/j.1365-246X.2012.05696.x

Kim, K., & Rodgers, A. (2016). Waveform inversion of acoustic waves for explosion yield estimation. *Geophysical Research Letters*, *43*(13), 6883–6890. https://doi.org/10.1002/2016GL069624

Kim, K., & Rodgers, A. (2017). Influence of low-altitude meteorological conditions on local infrasound propagation investigated by 3-D full-waveform modeling. *Geophysical Journal International*, *210*(2), 1252–1263. https://doi.org/10.1093/gji/ggx218

Kim, K., Rodgers, A., & Wright, M. (2018). Uncertainty analysis for infrasound waveform inversion: Application to explosion yield estimation. *Journal of the Acoustical Society of America*, *144*(6), 3351–3363. https://doi.org/10.1121/1.5082549

Krishnamoorthy, S., Komjathy, A., Pauken, M. T., Cutts, J. A., Garcia, R. F., Mimoun, D., et al. (2018). Detection of artificially generated seismic signals using balloon-borne infrasound sensors. *Geophysical Research Letters*, *45*, 3393–3403. https://doi.org/10.1002/2018GL077481

Krishnamoorthy, S., Lai, V. H., Komjathy, A., Pauken, M. T., Cutts, J. A., Garcia, R. F., et al. (2019). Aerial seismology using balloon-based barometers. *IEEE Transactions on Geoscience and Remote Sensing*, *1*, 11. https://doi.org/10.1109/TGRS.2019.2931831

Lacanna, G., & Ripepe, M. (2013). Influence of near-source volcano topography on the acoustic wavefield and implication for source modeling. *Journal of Volcanology and Geothermal Research*, *250*, 9–18. https://doi.org/10.1016/j.jvolgeores.2012.10.005

Lacanna, G., & Ripepe, M. (2020). Modeling the acoustic flux inside the magmatic conduit by 3D-FDTD simulation. *Journal of Geophysical Research: Solid Earth*, *125*(6), 1–18. https://doi.org/10.1029/2019JB018849

Lamb, O. D., Lees, J. M., & Bowman, D. C. (2018). Detecting lightning infrasound using a high-altitude balloon. *Geophysical Research Letters*, *45*, 7176–7183. https://doi.org/10.1029/2018GL078401

Lighthill, M. J. (1952). On sounds generated aerodynamically. I. General theory. *Proceedings of the Royal Society A, Mathematical, Physical and Engineering Science*, *211*(1107), 564–587.

Maher, S. P., Matoza, R. S., de Groot-Hedlin, C., Kim, K., & Gee, K. (2021). Evaluating the applicability of a screen diffraction approximation to local volcano infrasound. *Volcanica*, *4*, 67–85. https://doi.org/10.30909/vol.04.01.6785

Maher, S. P., Matoza, R. S., Groot-Hedlin, C. D., Gee, K. L., Fee, D., & Yokoo, A. (2020). Investigating Spectral Distortion of Local Volcano Infrasound by Nonlinear Propagation at Sakurajima Volcano, Japan. *Journal of Geophysical Research: Solid Earth*, *125*(3). https://doi.org/10.1029/2019jb018284

Martire, L., Martin, R., Brissaud, Q., & Garcia, R. F. (2021). SPECFEM2D-DG, an open source software modelling mechanical waves in coupled solid-fluid systems: The linearized Navier-Stokes approach. *Geophysical Journal International*, *228*, 1–19. https://doi.org/10.1093/gji/ggab308

Matoza, R. S., Fee, D., Green, D., & Mialle, P. (2019). Volcano infrasound and the international monitoring system. In A. L. Pichon, E. Blanc, & A. Hauchecorne (Eds.), *Infrasound monitoring for atmospheric studies* (pp. 1023–1077). Springer. https://doi.org/10.1007/978-3-319-75140-5_33

Matoza, R. S., Fee, D., Neilsen, T. B., Gee, K. L., & Ogden, D. E. (2013). Aeroacoustics of volcanic jets: Acoustic power estimation and jet velocity dependence. *Journal of Geophysical Research: Solid Earth*, *118*(12), 6269–6284. https://doi.org/10.1002/2013JB010303

Matoza, R. S., Garces, M. A., Chouet, B. A., D'Auria, L., Hedlin, M. A., De Groot-Hedlin, C., & Waite, G. P. (2009). The source of infrasound associated with long-period events at Mount St. Helens. *Journal of Geophysical Research*, *114*(4), 1–38. https://doi.org/10.1029/2008JB006128

McKee, K., Fee, D., Yokoo, A., Matoza, R. S., & Kim, K. (2017). Analysis of gas jetting and fumarole acoustics at Aso Volcano, Japan. *Journal of Volcanology and Geothermal Research*, *340*. https://doi.org/10.1016/j.jvolgeores.2017.03.029

Montalbetti, J. F., & Kanasewich, E. R. (1970). Enhancement of teleseismic body wave phases with a polarisation analysis. *Geophysical Journal of the Royal Astronomical Society*, *21*, 119–129.

Morse, P. M., & Ingard, K. U. (1986). *Theoretical acoustics*. Princeton University Press.

Ohminato, T., Chouet, B. A., Dawson, P. B., & Kedar, S. (1998). Waveform inversion of very-long-period impulsive signals associated with magmatic injections beneath Kilauea Volcano, Hawaii. *Journal of Geophysical Research*, *103*(10), 23839–23862. https://doi.org/10.1029/98JB01122

Ostashev, V. E., Wilson, D. K., Liu, L., Aldridge, D. F., Symons, N. P., & Marlin, D. (2005). Equations for finite-difference, time-domain simulation of sound propagation in moving inhomogeneous media and numerical implementation. *Journal of the Acoustical Society of America*, *117*(503). https://doi.org/10.1121/1.1841531

Paige, C. C., & Saunders, M. A. (1982). LSQR: An algorithm for Sparse linear equations and Sparse least squares. *ACM Transactions on Mathematical Software*, *8*(1), 43–71. https://doi.org/10.1145/355984.355989

Petersson, N. A., & Sjögreen, B. (2018). High order accurate finite difference modeling of seismo-acoustic wave propagation in a moving atmosphere and a heterogeneous earth model coupled across a realistic topography. *Journal of Scientific Computing*, *74*(1), 290–323. https://doi.org/10.1007/s10915-017-0434-7

Pierce, A. D. (1989). *Acoustics: An introduction to its physical properties and applications*. Melville, NY: Acoustical Society of America.

Rowell, C. R., Fee, D., Szuberla, C. A., Arnoult, K., Matoza, R. S., Firstov, P. P., et al. (2014). Three-dimensional volcano-acoustic source localization at Karymsky volcano, Kamchatka, Russia. *Journal of Volcanology and Geothermal Research*, *283*, 101–115. https://doi.org/10.1016/j.jvolgeores.2014.06.015

Wang, S. (1996). Finite-difference time-domain approach to underwater acoustic scattering problems. *Journal of the Acoustical Society of America*, *99*(4), 1924–1931. https://doi.org/10.1121/1.415375

Watson, L. M., Dunham, E. M., & Johnson, J. B. (2019). Simulation and inversion of harmonic infrasound from open-vent volcanoes using an efficient quasi-1D crater model. *Journal of Volcanology and Geothermal Research*, *380*, 64–79. https://doi.org/10.1016/j.jvolgeores.2019.05.007